Impact of 3D Cloud Structures on the Atmospheric Trace Gas Products from UV-VIS Sounders

ESA Contract No.: 4000124890/18/NL/FF/gp

TN-2:

Impact Assessment, Draft version

Claudia Emde[2], Huan Yu[3], Michel van Roozendael[3], Bernhard Mayer[2], Arve Kylling[1], and Kerstin Stebel[1]

[1]Norwegian Institute for Air Research (NILU), Kjeller, Norway
[2]Ludwig-Maximilians-University (LMU), Meteorological Institute, Munich, Germany
[3]Belgian Institute for Space Aeronomy (BIRA-IASB), Brussels, Belgium

June 22, 2019

Contents

1 Introduction

WP200 of the 3DCATS projects aims to estimate the bias of NO2 retrievals from Sentinel5 observations due to cloud scattering. The methodology is as follows: The 3D MYSTIC Monte Carlo radiative transfer model (Mayer, 2009; Emde et al., 2011) of the libRadtran package (Mayer and Kylling, 2005; Emde et al., 2016) is used to generate synthetic observations (spectra in the visible spectral range from 400-500nm and in the O2A band region from 755-775nm) for scenarios including 3D clouds. The NO2 retrieval algorithm (Blond et al., 2007; De Smedt et al., 2008) is applied to the synthetic data. Since the true NO2 concentration is known for the simulated scenes, the bias of the NO2 retrieval can then be calculated. Biases depending on cloud features shall be estimated and the most significant 3D cloud features shall be identified. In order to estimate the biases due to cloud scattering into clear regions and cloud shadowing, our first study is for a simple scene including a box-cloud. This allows us, to study the dependence of the bias on the following parameters: solar zenith angle, surface albedo, cloud optical thickness and cloud geometrical thickness. The NO2 retrieval algorithm includes two steps: first a DOAS fit is performed using the QDOAS software to get the NO2 slant column densities; second the slant column densities are converted to vertical column densities using air mass factors. The air mass factors are corrected for cloud scattering. The box-cloud scenario is also used to test the performance of a simplified treatment of clouds in the air mass factor calculations. In a follow-up study we plan to test the retrieval algorithm for scenes with well-defined sub-pixel clouds. Finally, we will generate a large data-set of synthetic observations for the typical cloud scenes defined in WP100 in order to get an estimation of the NO2 retrieval biases due to cloud scattering for real world observations.

2 Radiative transfer model intercomparison studies

2.1 Clear sky radiative transfer model intercomparison

Two radiative transfer models are used for the impact assessment of clouds on trace gas retrievals. The NO2 retrieval algorithm applies LIDORT (Spurr, 2006) as forward radiative transfer code. In order to generate synthetic observations for realistic three-dimensional cloud fields the MYSTIC model is used. As a first step we need to ensure that the retrieval works perfectly for 1D clear-sky cases, i.e. we have to check that the radiative transfer models agree for one-dimensional plane-parallel atmospheres.

2.1.1 Definition of setup

We include the US-standard atmosphere (Anderson 1986) with modified NO2 number concentration profiles, representative for a clean atmosphere over ocean (“Ocean”), a polluted atmosphere over ocean (“Pacific polluted”) and a polluted atmosphere over land (“European polluted”). These NO2 profiles are shown in Fig. 1.

Rayleigh scattering cross sections are calculated in both models using the parameterization by

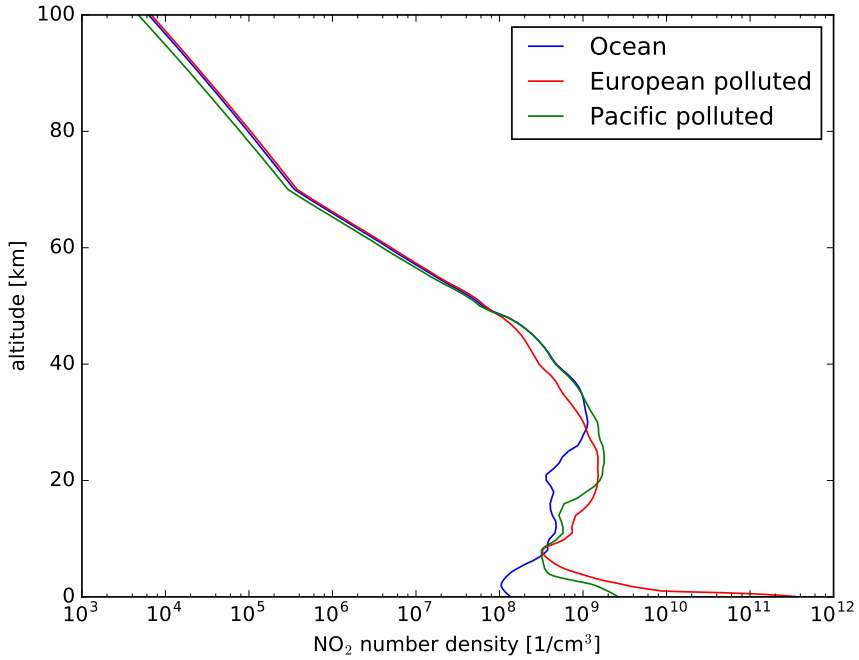

Figure 1: NO2 number concentration profiles for typical scenarios.

Bodhaine et al. (1999). For the visible spectral range from 400 to 500 nm we use the same absorption cross sections: NO_2 by Vandaele et al. (1998), O_3 by Serdyuchenko et al. (2014), O_4 by Thalman and Volkamer (2013).

For the O_2A-band region we performed line-by-line calculations with line parameters from the HITRAN2012 database for the midlatitude-summer standard atmosphere using the ARTS model (Eriksson et al., 2011). We use the resulting absorption coefficients as input to both radiative transfer models.

We performed simulations for various combinations of sun-observer geometries and surface albedos as summarized in the following table:

Surface albedo	0, 0.1, 0.3, 0.8
Solar zenith angle [°]	30, 60
Solar azimuth angle [°]	0
Viewing zenith angle [°]	0, 30, 60
Viewing azimuth angle [°]	0, 90, 180

Table 1: Parameters for clear-sky model intercomparison.

We have simulated radiances in spectral range from 400–500 nm with 0.2 nm resolution (VIS), and the range from 755–775 nm with 0.005 nm spectral resolution (O_2A band). Furthermore box airmass factors were calculated at 450 nm. The fine resolution in the O_2A band was chosen to resolve the individual spectral lines. For accurate simulation of Sentinel-5 observations, these spectra are convolved with the spectral response function.

2.1.2 Results for visible spectral range (400–500 nm)

Figs. 2–4 show the simulated clear-sky radiances for various cases. The base cases settings are given in the caption. In the first column the NO2 concentration is varied from the base case, in the second column the surface albedo, in the third column the solar zenith angle, in the fourth column the viewing zenith angle and in the last column the viewing azimuth angle. MYSTIC and LIDORT results shown Fig. 2 (nadir viewing, absorbing surface) agree very well, the relative difference is below 1% for all cases. Mostly, the results shown in Fig.3 also agree well, however there are some significant differences (about 4%) when the viewing azimuth angle is 180°. This sun-observer geometry corresponds to a scattering angle of 90°. This difference is likely due to small differences in the implementation of Rayleigh scattering. The cases shown in Fig. 4 agree well with relative differences smaller than about 2%. The differences are generally an offset over the full spectrum, this also indicates that the reason is a slightly different treatment of Rayleigh scattering. Absorption features agree perfectly.

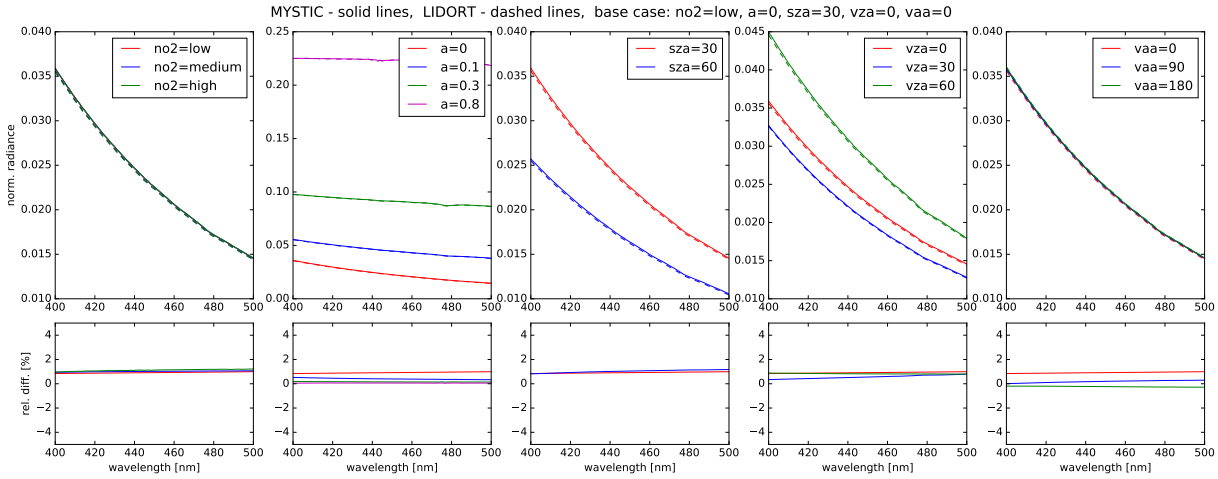

Figure 2: Radiance spectra for various parameters, the base cases settings are: low NO2 concentration (“Ocean”), surface albedo 0, solar zenith angle 30°, viewing zenith angle 0°(nadir) and viewing azimuth angle 0°. The upper panels show the normalized radiance (MYSTIC as solid lines and LIDORT as dashed lines) and the lower panels show the relative differences between the models.

Fig. 5 shows the simulated radiance at 400 nm for all 216 cases in the top panel. The LIDORT results plotted as red circles correspond well to the MYSTIC results plotted as blue circles. The lower panel shows the relative differences which is for the majority of the cases below 1%. As before, the larger differences are for sun-observer geometries with a scattering angle of 90°.

Figs. 6 and 7 show the comparison of simulated box-airmass factors. The agreement between the models is good as can be seen in the upper panels. The relative differences reveal some noise from the Monte Carlo simulation and in addition also some systematic deviations, which we again attribute to a slightly different Rayleigh scattering treatment.

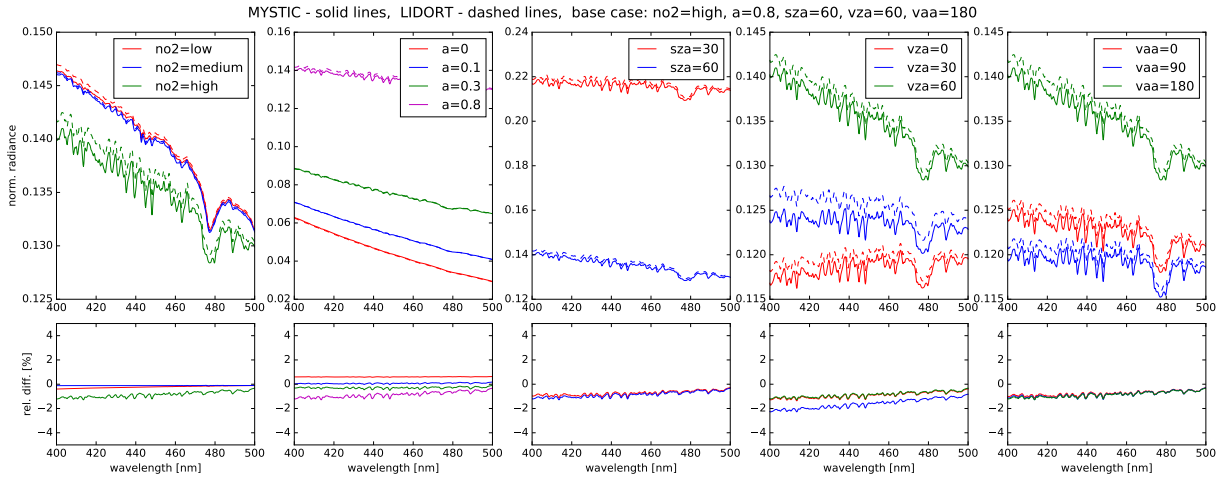

Figure 3: Radiance spectra for various parameters, the base cases settings are: high NO2 concentration (“European polluted”), surface albedo 0.8, solar zenith angle 60°, viewing zenith angle 60°(nadir) and viewing azimuth angle 180°. The upper panels show the normalized radiance (MYSTIC as solid lines and LIDORT as dashed lines) and the lower panels show the relative differences between the models.

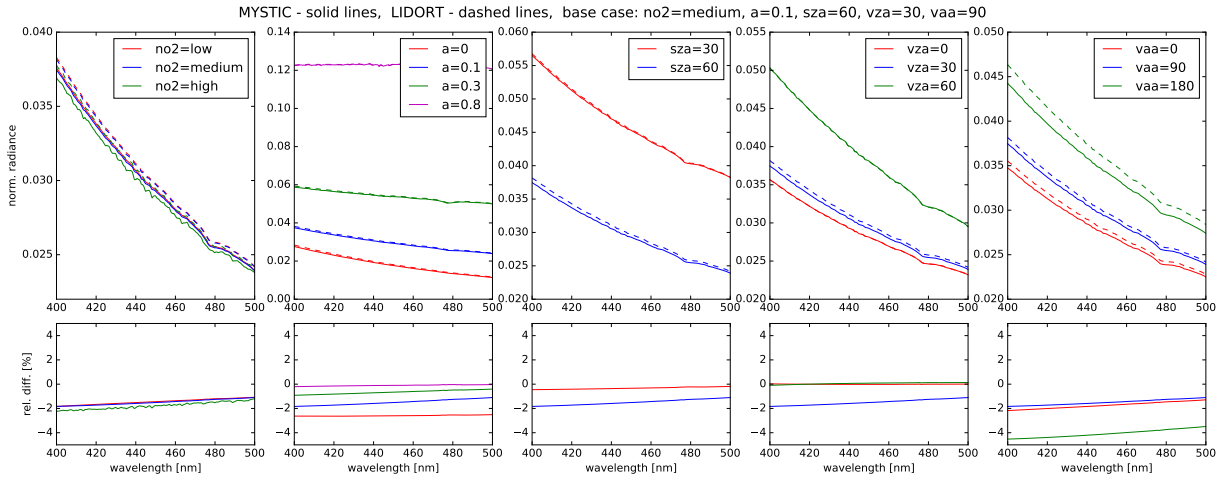

Figure 4: Radiance spectra for various parameters, the base cases settings are: medium NO2 concentration (“Pacific polluted”), surface albedo 0.1, solar zenith angle 60°, viewing zenith angle 30°(nadir) and viewing azimuth angle 90°. The upper panels show the normalized radiance (MYSTIC as solid lines and LIDORT as dashed lines) and the lower panels show the relative differences between the models.

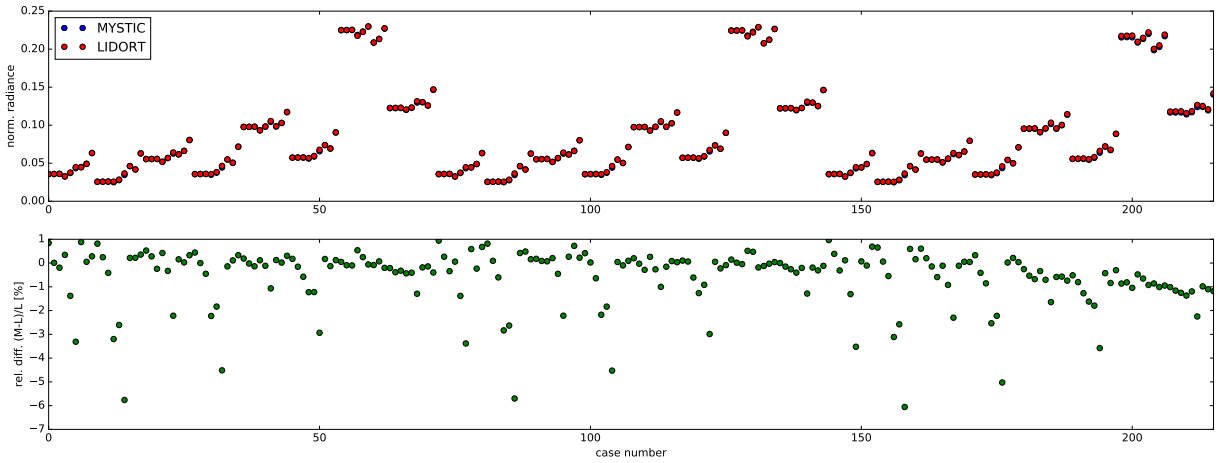

Figure 5: Normalized radiance and relative differences at 400 nm for all 216 cases.

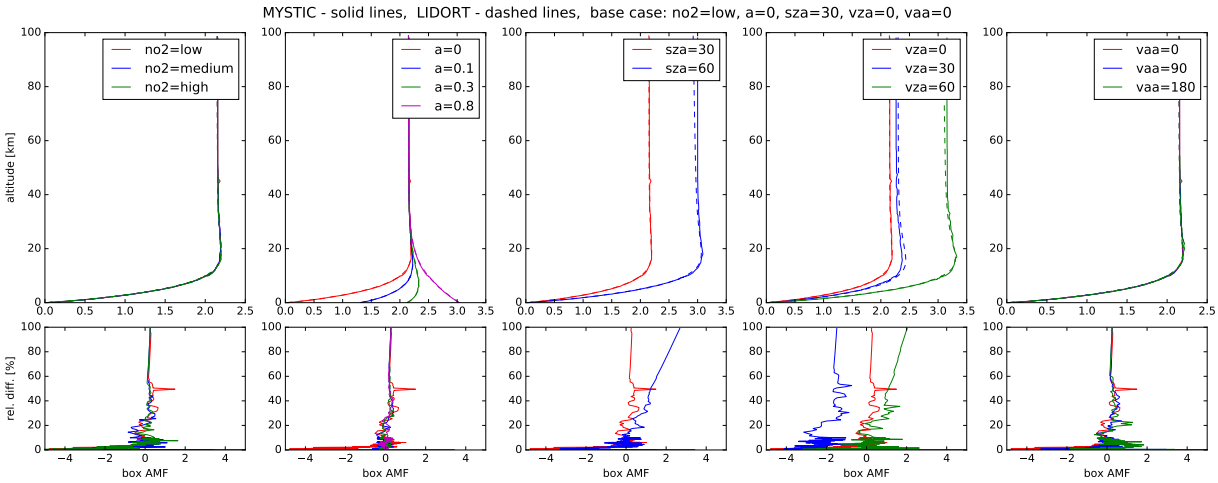

Figure 6: Dependence of the box airmass factor on various parameters. The base cases settings are: low NO2 concentration (“Ocean”), surface albedo 0, solar zenith angle 30°, viewing zenith angle 0°, and viewing azimuth angle 0°. The upper panels show MYSTIC and LIDORT results and the lower panels the relative differences.

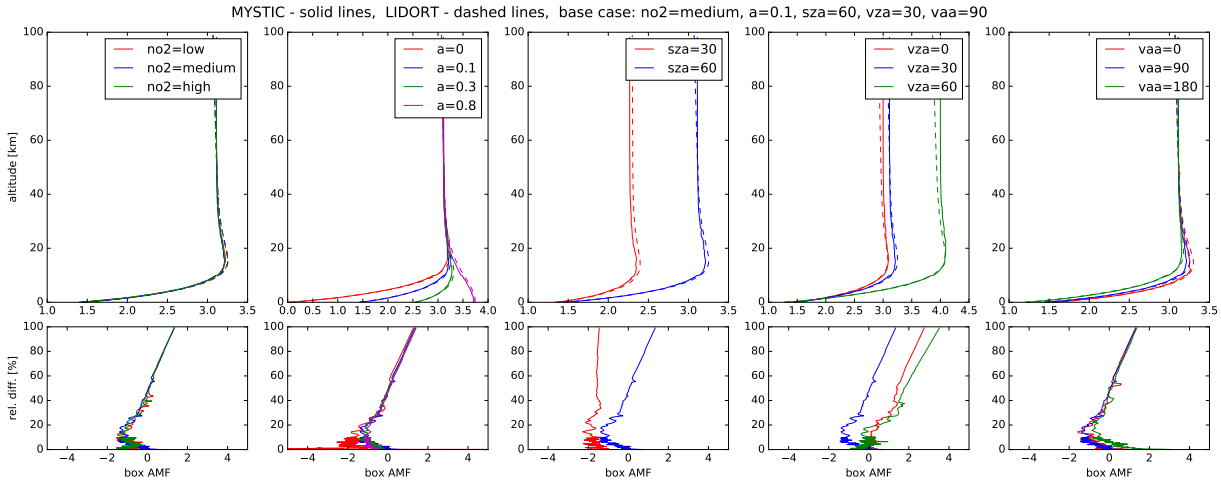

Figure 7: Dependence of the box airmass factor on various parameters. The base cases settings are: low NO2 concentration (“Pacific polluted”), surface albedo 0, solar zenith angle 60°, viewing zenith angle 30°, and viewing azimuth angle 90°. The upper panels show MYSTIC and LIDORT results and the lower panels the relative differences.

2.1.3 Results in O_2A-band (755–775 nm)

Fig. 8 shows results in the O2A-band region for selected cases. The relative difference between the models is smaller than 1% in the continuum. It becomes larger in absorption line centers since the normalized radiances is close to 0. Fig. 9 shows the region from 767–768 nm, here we see that individual absorption lines are well resolved for both models.

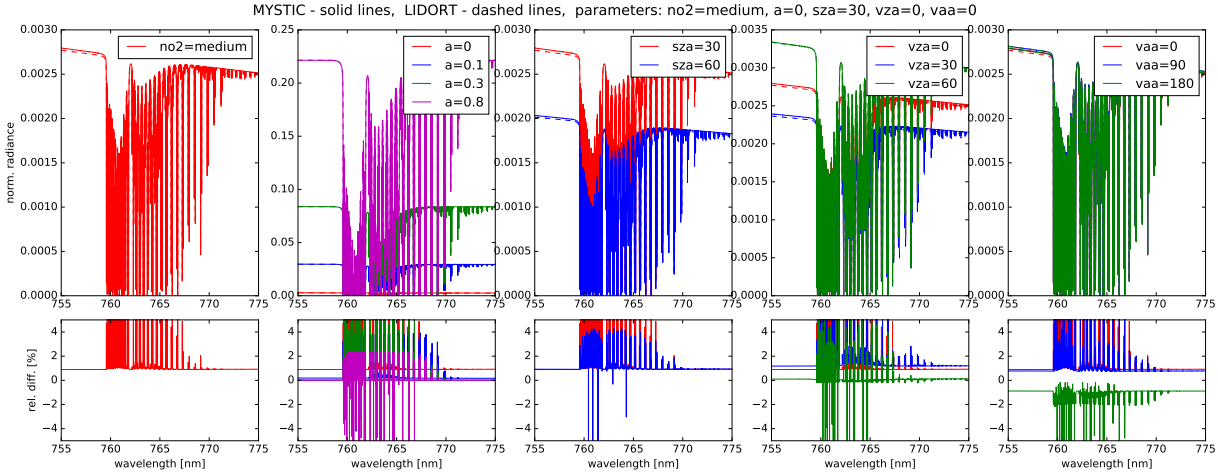

Figure 8: Spectral radiance in O_2A-band simulation with a spectral resolution of 0.005 nm, the base case settings are: NO2 concentration from midlatitude summer atmosphere, surface albedo 0, solar zenith angle 30°, viewing zenith angle 0°and viewing azimuth angle 0°. The upper panels show the normalized radiance (MYSTIC as solid lines and LIDORT as dashed lines) and the lower panels show the relative differences between the models.

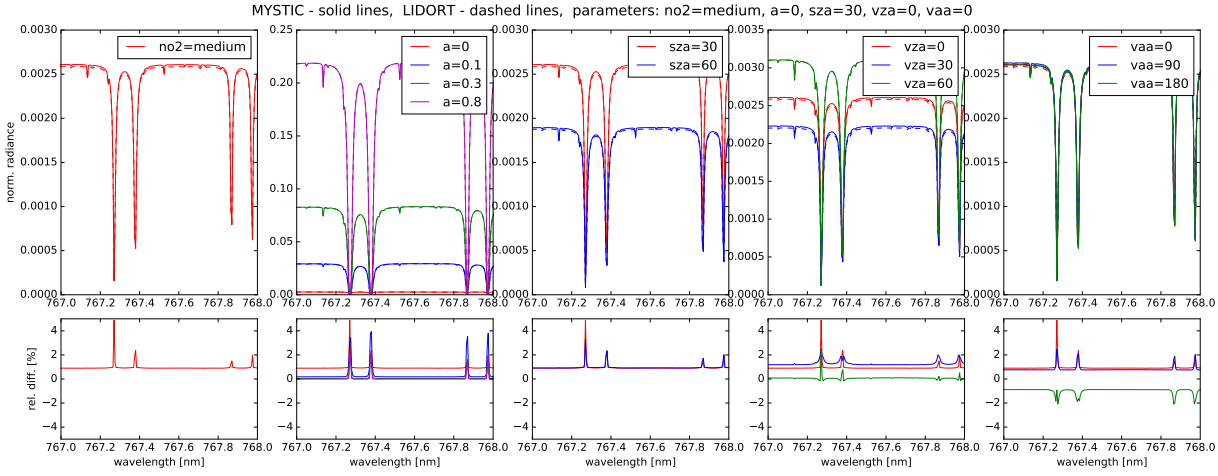

Figure 9: As Fig. 8, zoomed into narrow wavelength region from 767.0 to 768.0 nm.

Fig. 10 shows the results for all cases at 755 nm. We find that the relative difference between the models is mostly below 1%, except for a few outliers for specific sun-observer geometries.

The left panel in Fig. 11 shows the O_2A-band region convolved with the Sentinel-5 spectral response function for various sun-observer geometries calculated with MYSTIC and LIDORT,

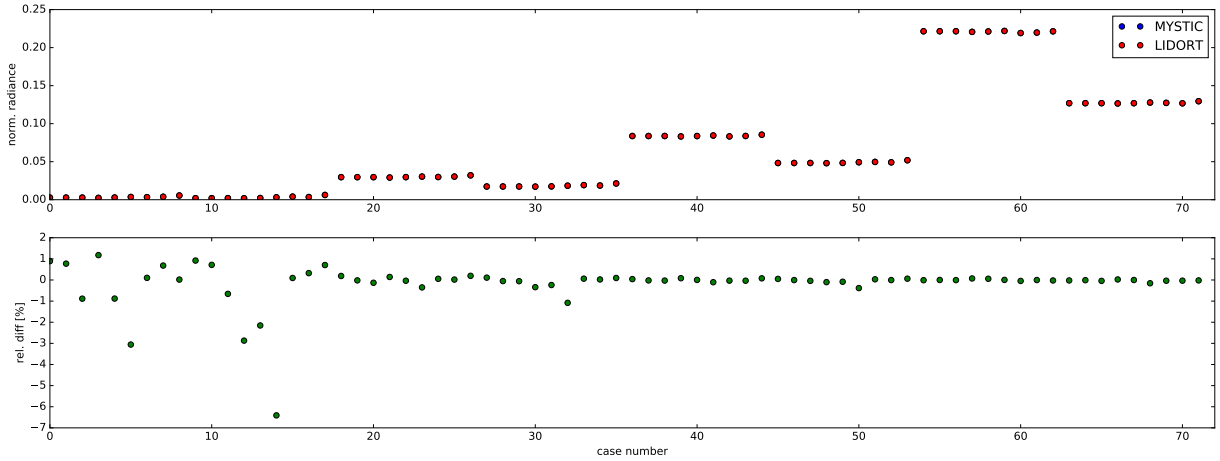

Figure 10: Normalized radiance and relative differences between MYSTIC and LIDORT at 755 nm for all cases.

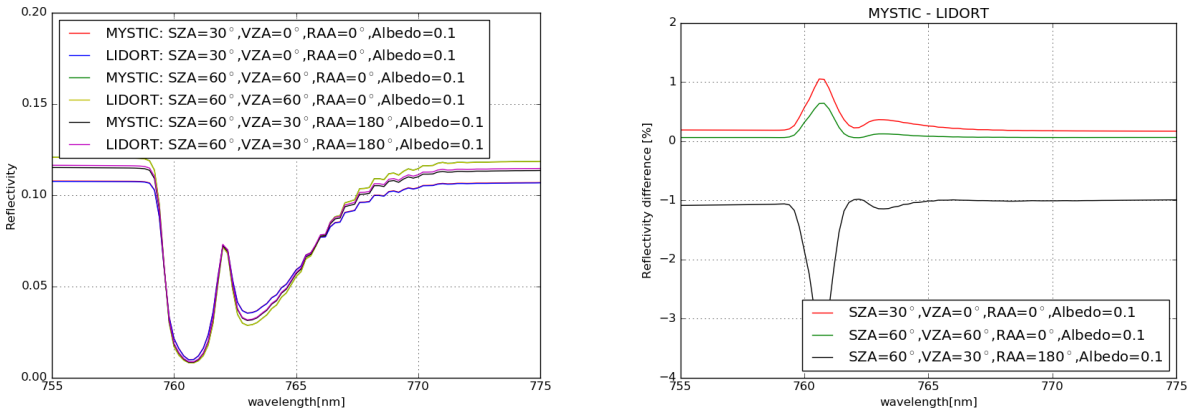

Figure 11: *Left:* Convolved spectra calculated from high spectral resolution simulations with MYSTIC and LIDORT for various sun-observer geometries. *Right:* Relative differences between MYSTIC and LIDORT.

respectively. The right panel shows the relative differences which are below about 1% for most geometries. However for the problematic geometries with scattering angles about 90° it is up to about 3% in the O_2A-absorption band.

2.2 Model intercomparision for 1D plane-parallel clouds

The cloud correction algorithm of the NO2 retrieval uses LIDORT radiative transfer simulations with 1D layered clouds. Thus, we need to check, whether for 1D clouds, the models MYSTIC and LIDORT are consistent. We use the same atmospheric and sun-observer geometries as in the clearsky intercomparison and include a cloud layer in addition. The cloud optical thickness is varied between 1 and 20 and the cloud base height between 1 and 10 km. MYSTIC results have been provided and are currently compared to LIDORT.

2.3 Impact of model differences on NO_2 retrieval

In the NO_2 retrieval, the discrepancy between LIDORT and MYSTIC simulation will affect the DOAS fit in the slant column, the box-AMF and the cloud correction in the AMF calculation. Figure 12 shows that the use of MYSTIC and LIDORT simulated spectrum lead to up to 2.5% difference in the DOAS fit. The box-AMF calculated by two radiative transfer models contributes 4% bias in the calculation of the total AMF. Finally, it will introduce up to 5% bias in the NO_2 retrieval.

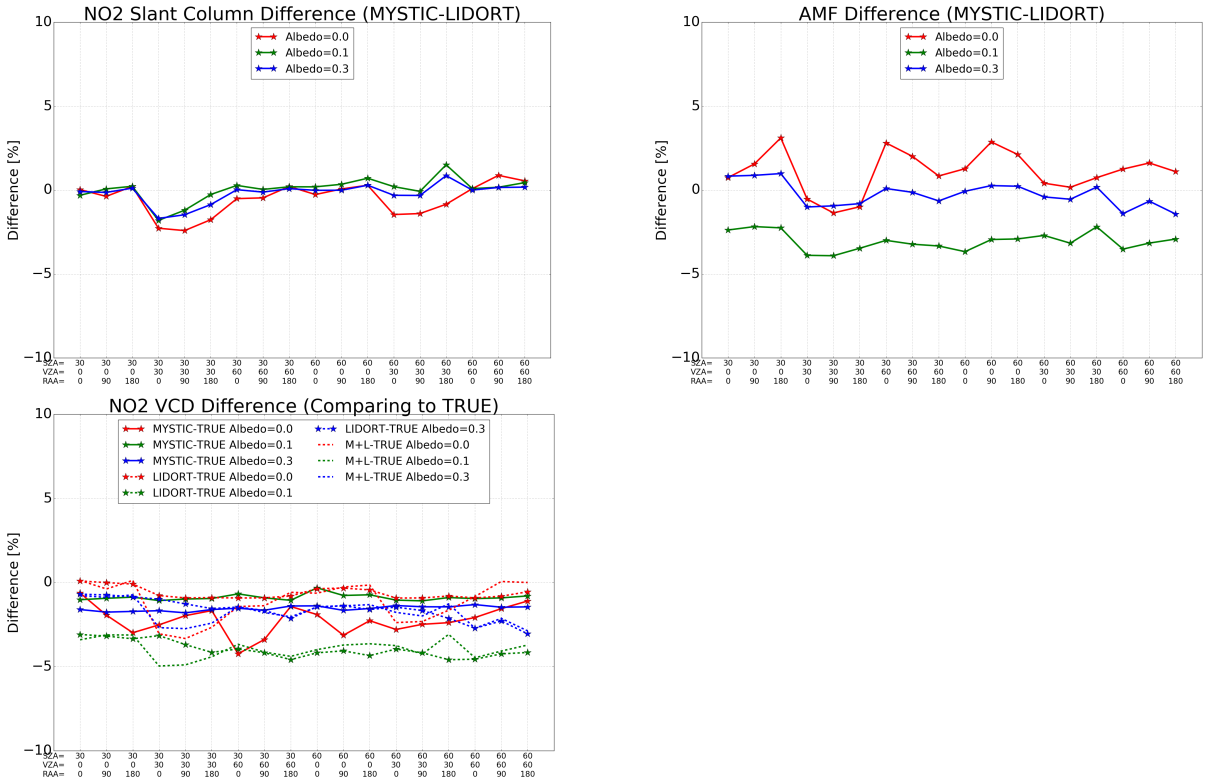

Figure 12: Model intercomparison for the NO_2 retrieval. *Top left:* difference of NO_2 slant column retrieval between the use of spectrum simulated by MYSTIC and LIDORT; *top right:* total AMF difference using box-AMF calculated by MYSTIC and LIDORT, the true profile is used for the calculation of total AMF; *bottom left:* effect on the NO_2 retrieval for varieties of settings (solid line: slant column from MYSTIC simulated spectrum, AMF using box-AMF from MYSTIC simulation; dash line: slant column from LIDORT, AMF using box-AMF from LIDORT; dot line: : slant column from MYSTIC, AMF using box-AMF from LIDORT)

The other important aspect is about cloud retrieval and its impact on the AMF calculation. Both O2-O2 and O2-A (so-called FRESCO algorithm) cloud retrieval algorithms are using LIDORT as the forward simulator, and applying to the MYSTIC simulated spectrum.

Figure 13 shows good agreement in cloud fraction between two algorithms, FRESCO cloud fraction slightly higher, especially for high COT cases, probably due to the difference in Rayleigh scattering between two bands. There is an outlier for the geometry with SZA/VZA=60°, RAA=0°, the retrieved cloud fraction is systematically higher than the other geometries, probably because of a large discrepancy between LIDORT and MYSTIC simulation. The O2-O2 cloud fraction is higher than FRESCO, mainly due to a constraints in FRESCO cloud retrieval, and cloud fraction is limited on the range of [0, 1].

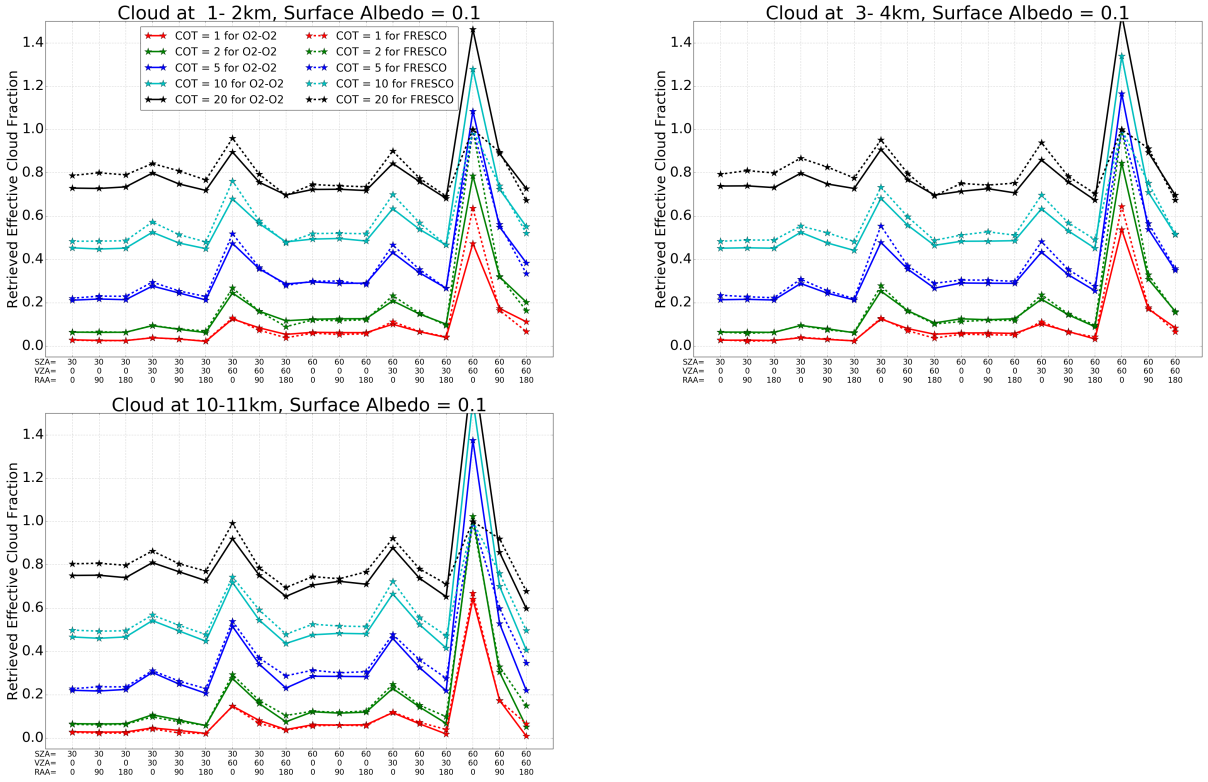

Figure 13: Comparison of effective cloud fraction retrieval at O2-O2 and O2-A band for surface albedo 0.1, cloud height 1-2km (top left), 3-4km (top right) and 10-11km (bottom left). Solid line is O2-O2 cloud fraction, and dash line is FRESCO cloud fraction, varies of colors represent the different cloud optical thickness.

The cloud height retrieval shows relatively larger differences (Figure 14). O2-O2 cloud height usually is close to the middle of true cloud layer, and decreases with decreasing of cloud optical thickness, large variations in cloud height retrieval can be found for high cloud cases, since the O2-O2 cloud algorithm is less sensitive in high cloud than low cloud. FRESCO cloud height is systematically lower than O2-O2.

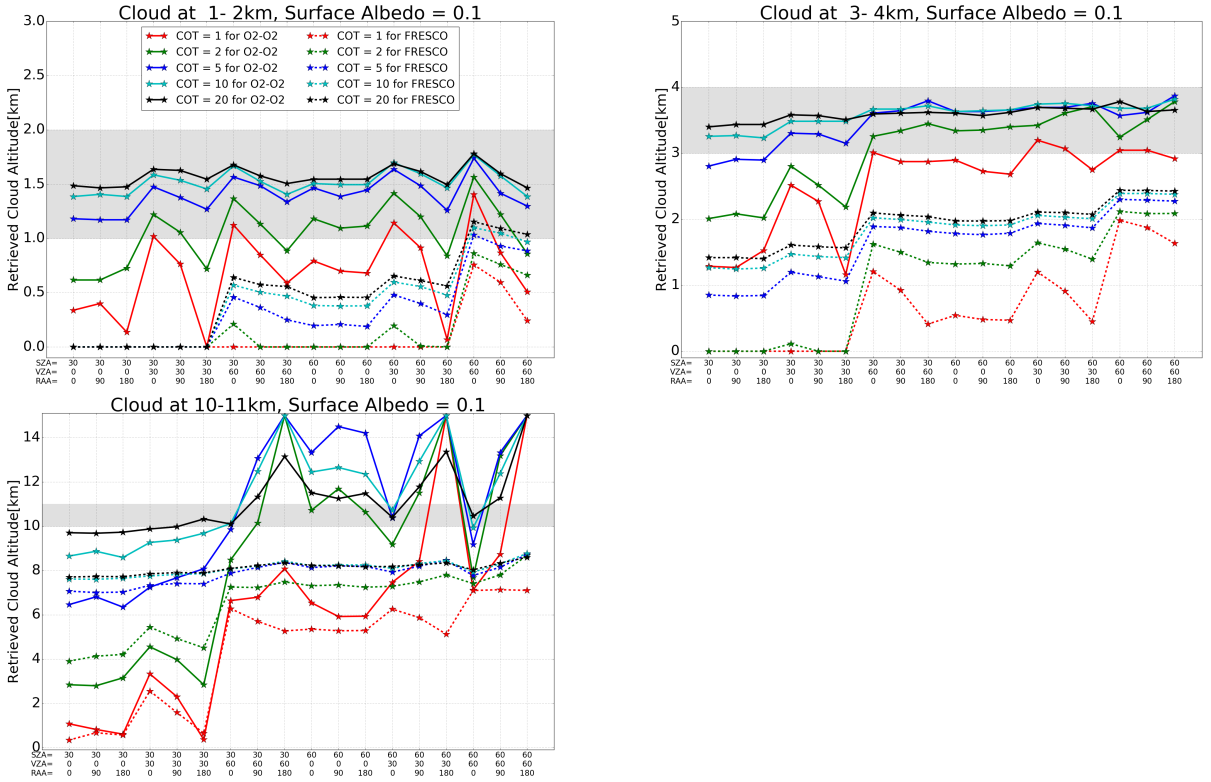

Figure 14: Comparison of cloud height retrieval at O2-O2 and O2-A band for surface albedo 0.1, cloud height 1-2km (top left), 3-4km (top right) and 10-11km (bottom left). Solid line is O2-O2 cloud height, and dash line is FRESCO cloud height, varies of colors represent the different cloud optical thickness.

Finally, the AMF calculation is corrected by the retrieved cloud property, and comparing the true AMF from MYSTIC (Figure 15). Please note that the differences are caused by two factors: box-AMF difference between MYSTIC and LIDORT simulation, and the simplified cloud correction for AMF. As discussed above (Figure 12), the influence of first factor is small, therefore, the difference is mainly due to the cloud correction. Results show that the effect is mostly within 20%, a few outliers are found when AMF using FRESCO correction for low cloud cases, since the retrieved FRESCO cloud height is close to surface level, and introducing a large error in the AMF calculation. The bias at SZA/VZA/RAA = 60°/60°/0°is linked to the discrepancy in the cloud fraction retrieval.

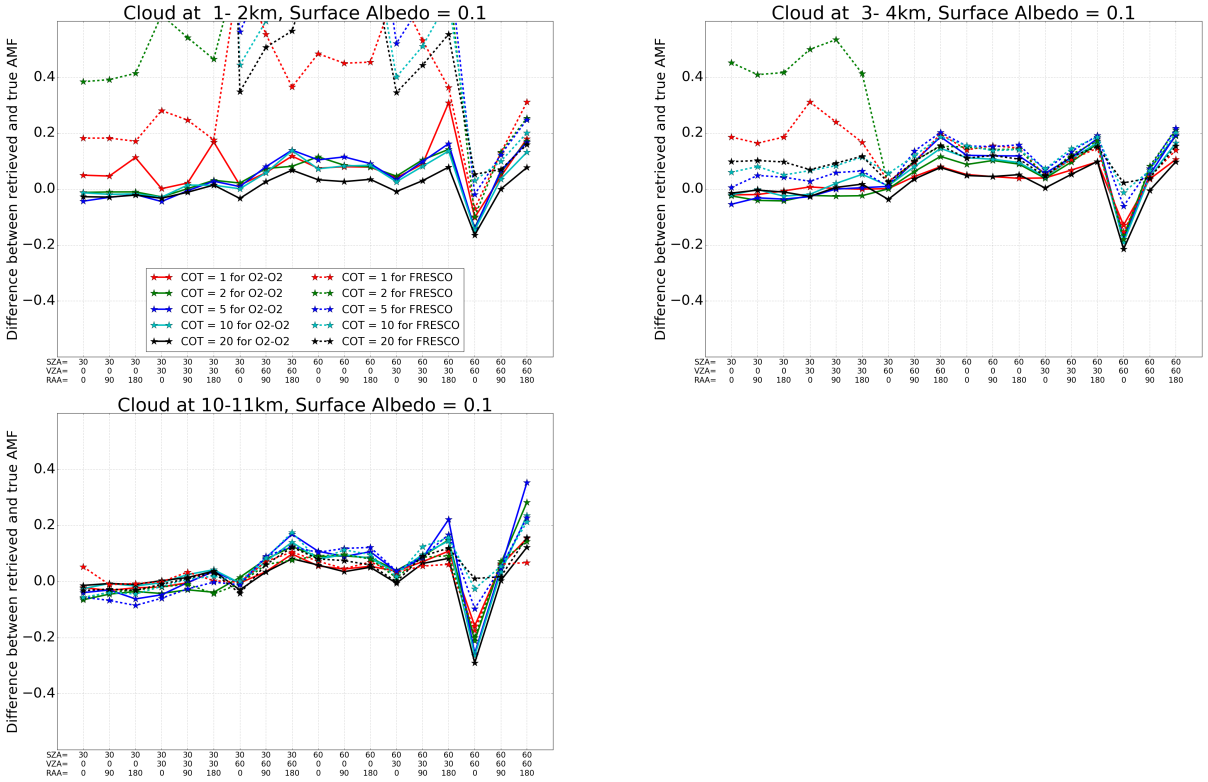

Figure 15: Comparison of AMF calculation using the cloud correction based on cloud retrieval at O2-O2 and O2-A band for surface albedo 0.1, cloud height 1-2km (top left), 3-4km (top right) and 10-11km (bottom left). Solid line is AMF using O2-O2 cloud correction, and dash line is AMF using FRESCO cloud correction, varies of colors represent the different cloud optical thickness.

3 Retrieval of NO_2 for clearsky pixels in the vicinity of clouds

3.1 Setup of box-cloud scenario

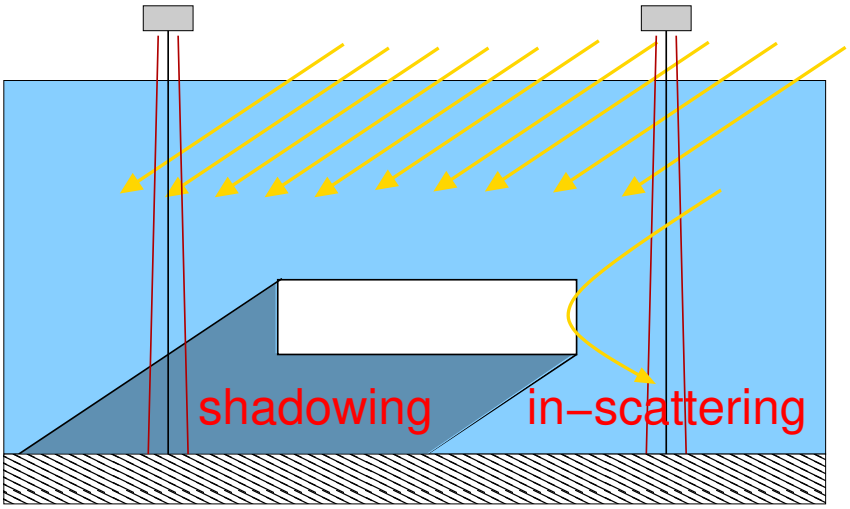

Figure 16: Schematic of box-cloud scenario.

In order to investigate the effect of cloud scattering or shadowing in clear regions near clouds we start with a simple setup including a box-cloud, as depicted in Fig. 16.

We included the midlatitude summer standard atmosphere in our model and used the NO2 number concentration profiles named “Pacific polluted” and “European polluted” (see Fig. 1).

The box-cloud is defined as follows: the cloud base height is 2 km and the cloud top height 3 km. The cloud droplet effective radius is assumed to be 10 μm, a typical value for liquid water clouds. We further assumed a gamma size distribution with an effective variance of 0.1 for the cloud droplets and calculated the optical properties using the Mie tool provided with libRadtran. The cloud optical thickness is set to 10 for the base case scenario. We performed simulations for a nadir viewing sensor with a 1x1km^2 field-of-view, similar to MODIS. The solar zenith angle is set to 50° and the surface albedo to 0.05. Aerosols were not included in this setup.

Fig. 17 shows the simulated reflectance as a function of distance from the cloud edge. Negative distances with lower reflectance values correspond to clear pixels and positive distances correspond to cloudy pixels. The dashed lines correspond to clear sky simulations. Near the cloud edge (between 0 and about -3 km) we can clearly see the influence of the cloud: the reflectance is increased, when the sensor “looks” at the illuminated side of the cloud (left panel) and is decreased in the cloud shadow (right panel). Also for cloudy pixels (positive distances) the reflectance is not constant, it is higher on the illuminated cloud side and lower on the shadow side.

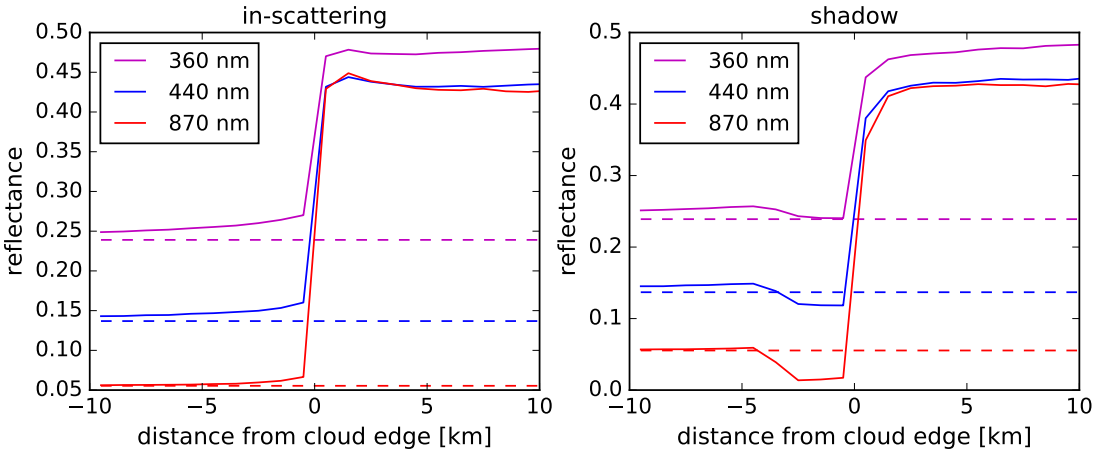

Figure 17: Reflectance as a function of distance from the cloud edge at wavelengths of 360 nm, 440 nm and 870 nm. Negative values correspond to clear pixels, positive values correspond to cloudy pixels. The left panel shows the enhancement due to scattering into the clear region. The right panel shows the cloud shadow. The dashed lines correspond to clear sky reflectances.

3.2 Three-dimensional box-airmass-factors

MYSTIC includes the capability to compute three-dimensional box-airmass-factors (3D box-AMF), which may help us to understand the influence of the clouds. Fig. 18 shows the 3D box-AMF for clear sky for the base case settings defined above. Our setup is 2D, i.e. all quantities are constant in y-direction. The sensor is placed at the top of the atmosphere and the viewing direction is nadir. The field-of-view is 1 km^2 and it ranges in x-direction from 98–99 km. The box-airmass-factor gives the contribution of a model box to the reflectance. The largest values are found on a vertical line between observer and surface, along the observation direction. The slant line corresponds to the connection between surface and sun. The right panel in Fig. 18 shows the integral of the 3D box-AMF over horizontal layers, this corresponds to the common 1D box-AMF, which should be called more precisely "layer-AMF". The bottom panel shows the integral over vertical layers. Here we see that the major contribution to the reflectance results from horizontal distances of up to about 8 km from the sensor, this distance increases with increasing solar zenith angle.

Fig. 19 shows the 3D box-AMF for a domain including a 2D cloud which starts at x=100 km, thus 10 km away from the FOV of the sensor. The difference between left and right panel is the solar azimuth angle, on the left the sun is on the same side as the cloud and on the right it is on the opposite side. The 2D plots clearly show, that photons, which are scattered at the cloud side into the FOV contribute to the reflectance. However, quantitatively this contribution is relatively small, as can be seen in the integrated box-AMFs, which are not much different from the clear sky results, and in Fig 20 showing the differences between cloud and clearsky setup.

Fig. 21 shows the 3D box-AMF, for a cloud being only 1 km away from the FOV. Thus, the left panel corresponds to an observation of the cloud shadow. The "slant line" between surface and sun is not visible in the 3D box-AMF because photons can not directly reach the surface at the location of the FOV. The layer-AMF (right panel) differs strongly from the clear-sky, there is

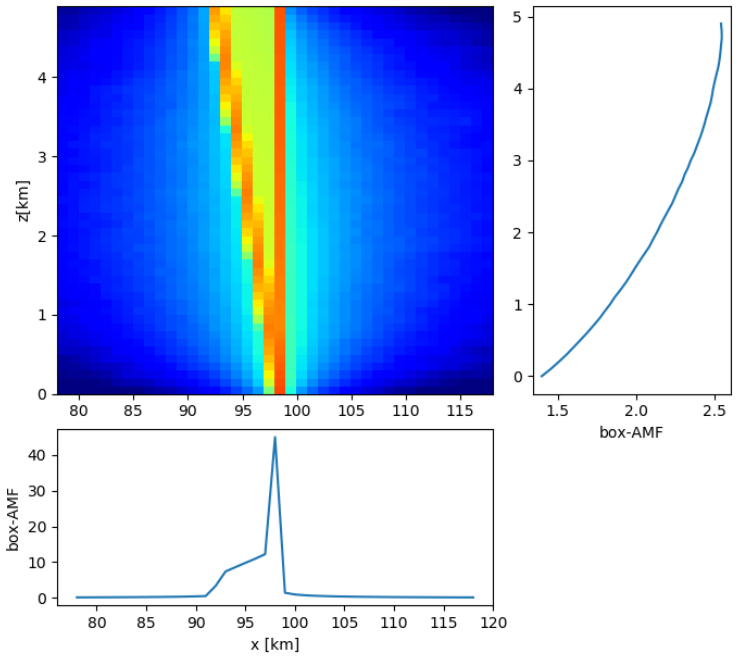

Figure 18: 3D box-AMF at 440 nm for clear-sky. The right panel shows the integrated box-AMF over the horizontal layers ("layer-AMF"). The bottom panel shows the integrated box-AMF over vertical layers.

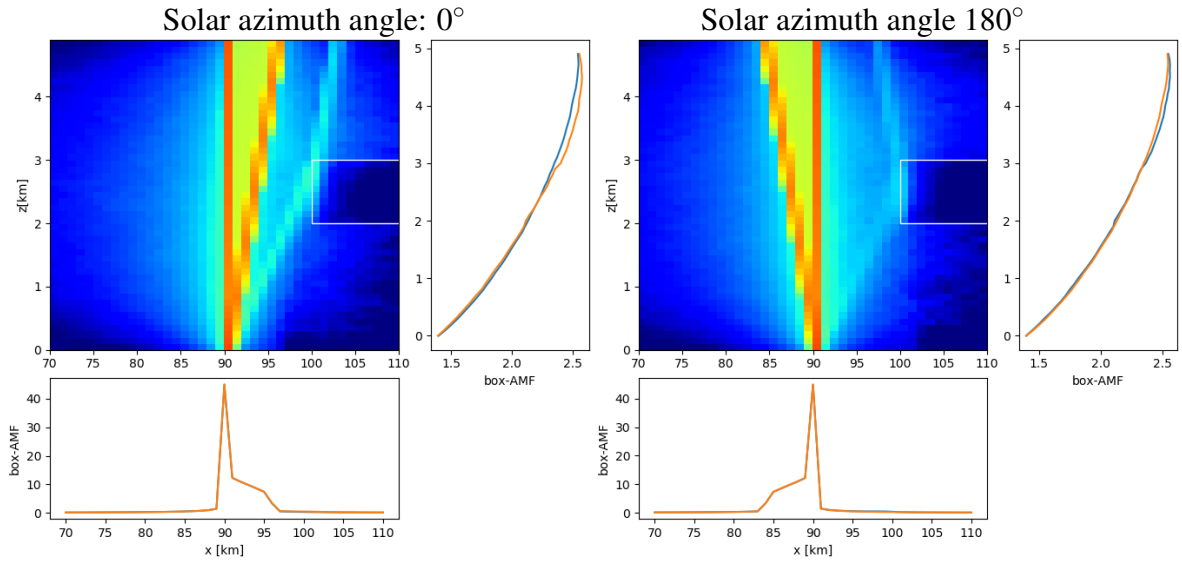

Figure 19: Same as Fig. 18 but including the box-cloud. The field-of-view of the nadir viewing sensor is 10 km away from the cloud edge. Left and right panels are for different solar azimuth angles. The blue lines in the figures showing integrated box-AMFs are for clearsky and the orange lines include the clouds.

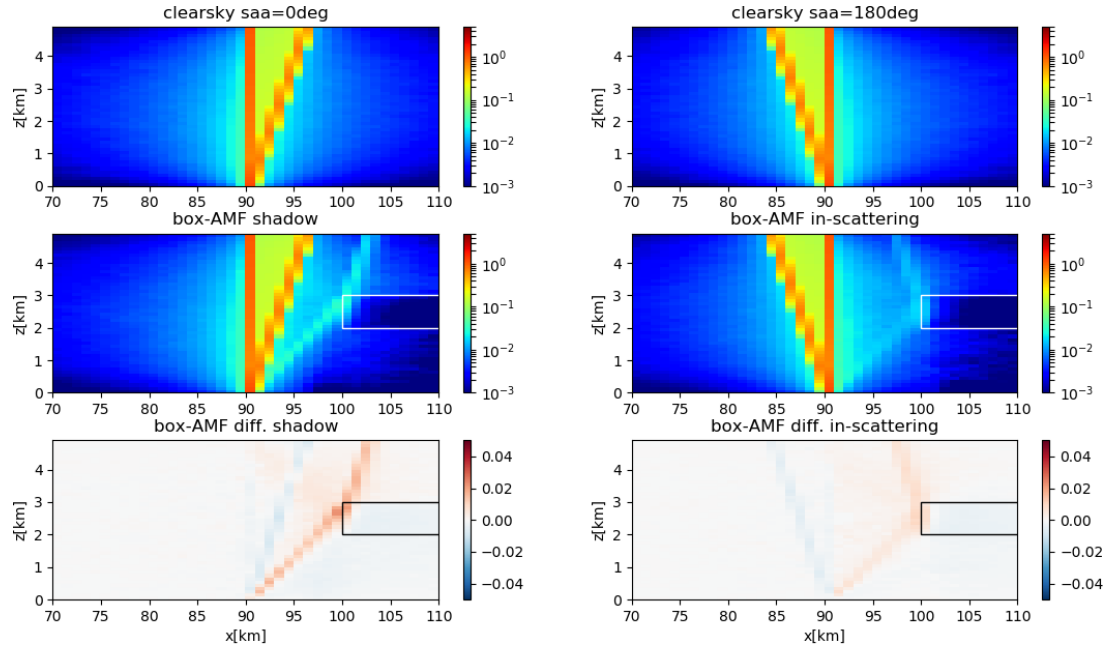

Figure 20: *Top panels:* Clear-sky box-AMF. *Middle panels:* Box-AMFs including box-cloud at 10 km distance from sensor's field of view. *Bottom panels:* Difference between clearsky and cloudy box-AMFs.

much less contribution to the reflectance from altitudes below the cloud. On the right panel, the sun comes from the other side, thus the FOV is not in shadow. Here the influence on box-AMFs is comparatively small. The differences between clearsky and clouds box-AMFs are shown in Fig. 22.

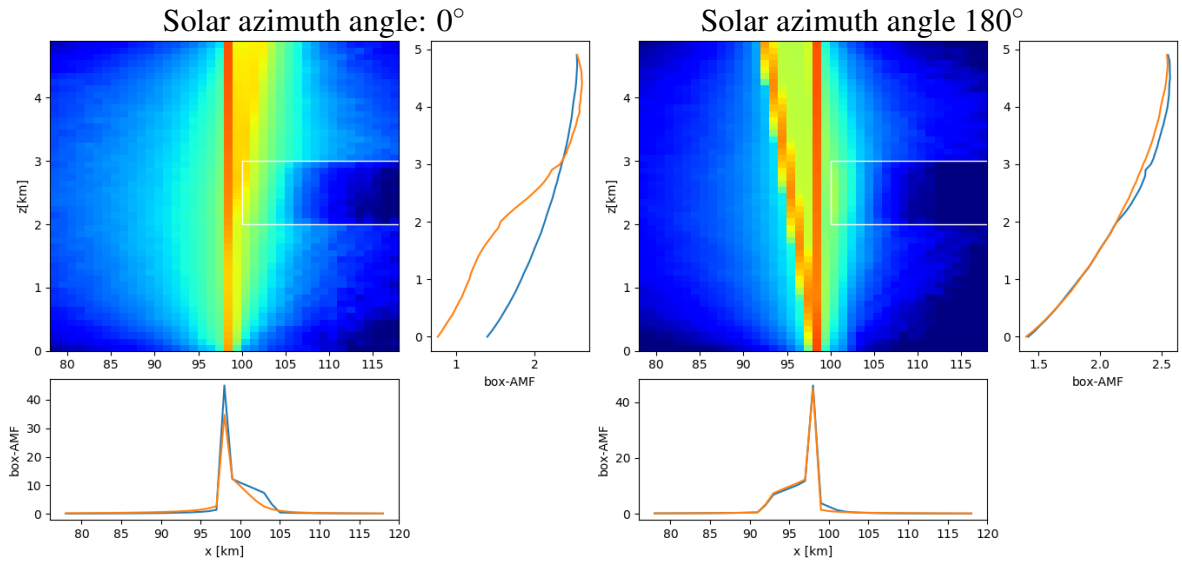

Figure 21: Same as Fig. 20 for the FOV being only 1 km away from cloud edge.

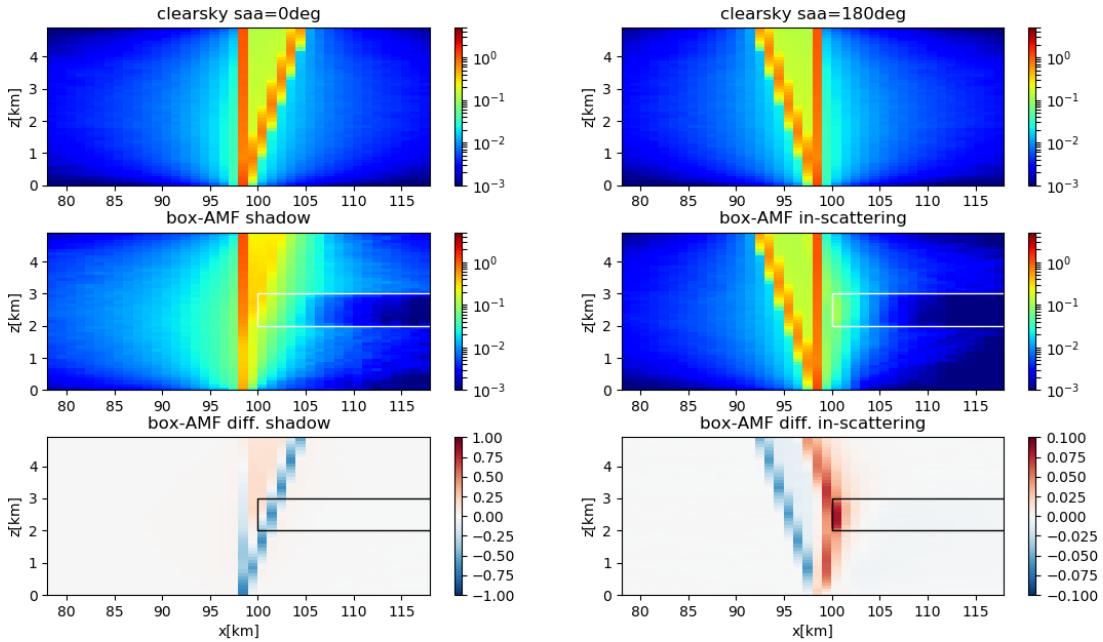

Figure 22: *Top panels:* Clear-sky box-AMF. *Middle panels:* Box-AMFs including box-cloud at 1 km distance from sensor's field of view. *Bottom panels:* Difference between clearsky and cloudy box-AMFs.

3.3 Simulated reflectance spectra and differential optical thickness

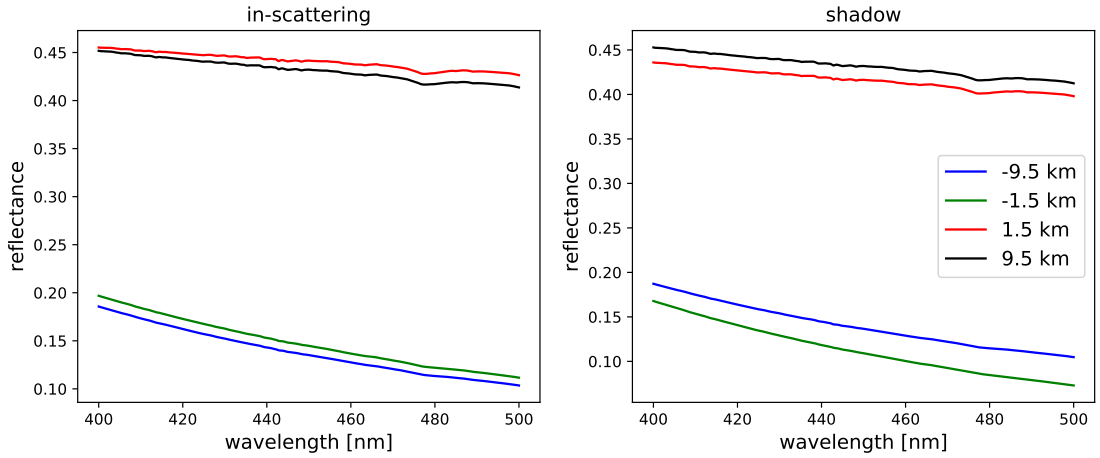

Figure 23: Simulated reflectance spectra for the visible spectral range at different locations. The legend denotes the respective distances from the cloud edge.

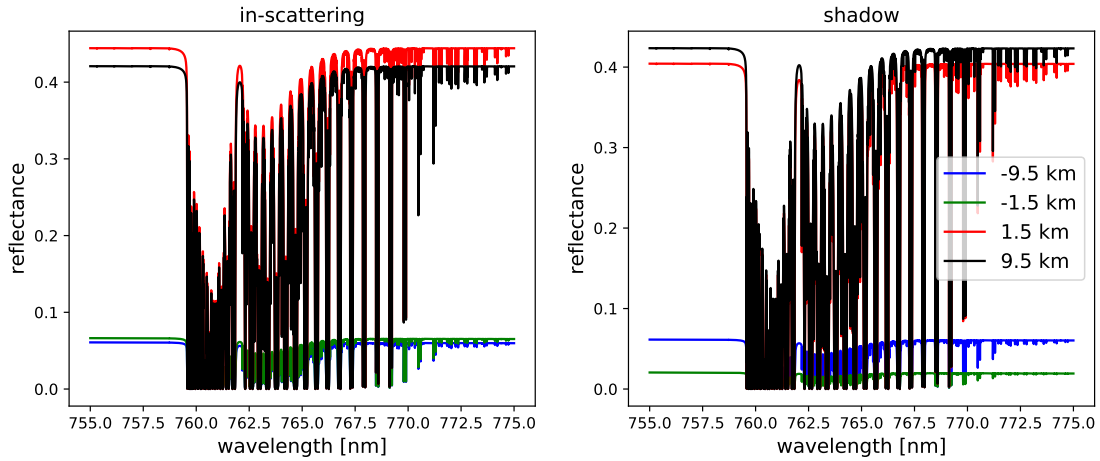

Figure 24: Simulated reflectance spectra for the O_2A-band at different locations. The legend denotes the respective distances from the cloud edge.

Fig. 23 shows reflectance spectra at different positions with respect to the cloud edge. The red and the black curve represent spectra for the cloudy part and the blue and the green lines are for the clearsky part. The green line corresponds to the pixel ranging from 1-2km distance from the cloud edge. (The simulated "pixels" are of size 1x1 km^2 and the reflectance avaraged over such pixels is equivalent to reflectance averaged over a FOV of 1x1 km^2). The blue line is for the pixel ranging from 9-10km distance, therefore this is similar to a clear pixel with almost no cloud influence. We see that on the illuminated side, the overall spectrum is increased and in the shadow it is decreased. For the O_2A band region (see Fig. 24), the cloud brightening effect is very small. The cloud shadow is clearly visible also in this spectral region.

In order to get a first impression, whether the cloud can have an impact on the NO2 retrieval, we have derived the differential optical thickness (DOD) from the VIS spectra (see Fig. 25). The

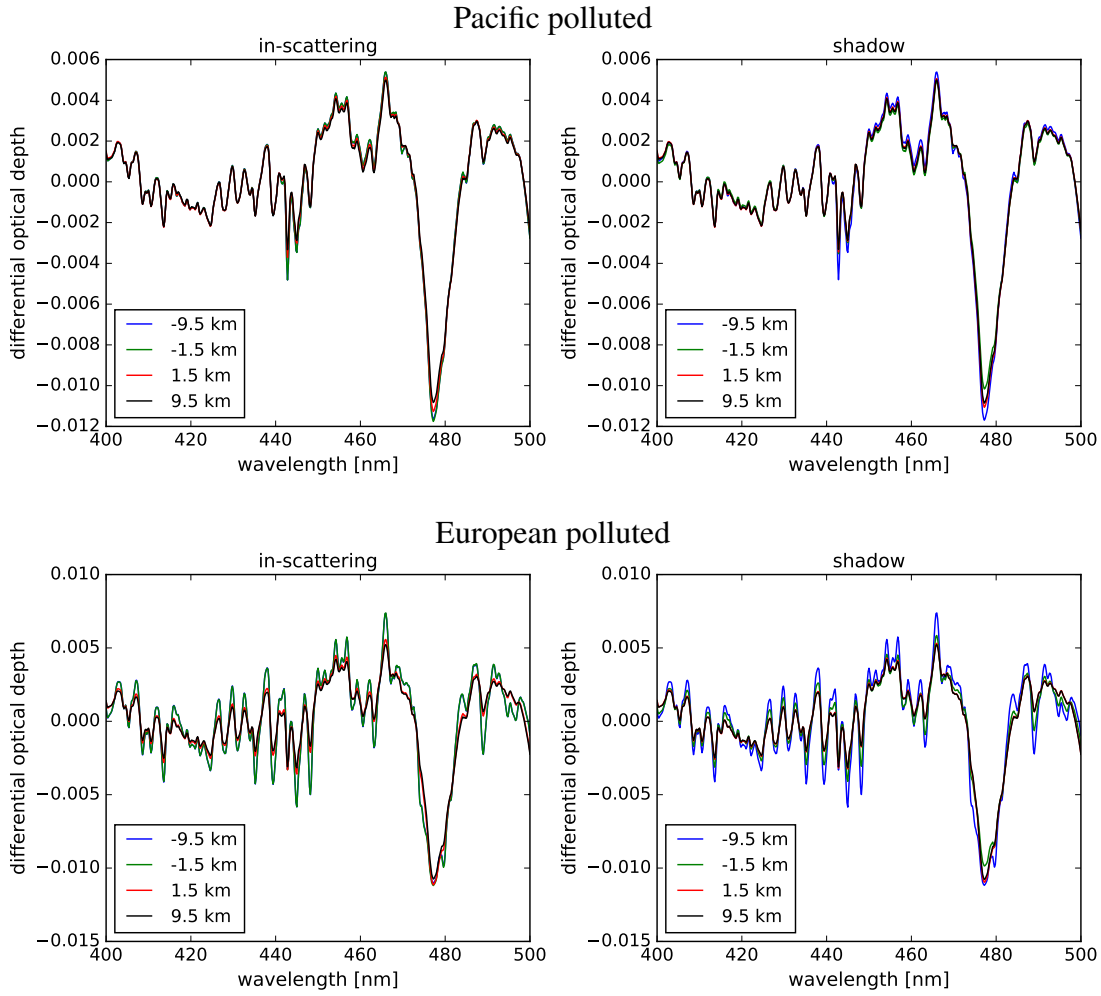

Figure 25: Differential optical thickness for pixels in clear region (blue and green) and cloudy region (red and black). The left panels show pixels with radiation scattered into the clear region and the right panels show the cloud shadow (-1.5 km away from cloud edge). The upper panels are for the Pacific polluted case, the lower panels for the European polluted case.

upper panels correspond to the Pacific polluted case, and the lower panels correspond to the European polluted case. We find that the differential optical thickness is not much influenced by the cloud for the Pacific polluted case. The obvious reason is, that the largest part of the NO2 molecules are found in altitudes above the cloud layer (compare Fig. 1). For the European polluted case, where the largest part of the NO2 is situated in the atmospheric boundary layer below the cloud, we find that the diffential optical thickness is much influenced by the cloud. In particular it is different for the pixels near the cloud edge (-1.5 km, green line) compared to pixels further away from cloud edge (-9.5 km, blue line). The retrieved NO_2-concentration depends on the depth of the absorption features in the DOD. When we look at the blue and the green lines in the right panels of Fig. 25, we see that for the European polluted profile, the absorption features are much stronger for the blue lines compared to the green line, thus the retrieved NO_2 concentration will be smaller in the cloud shadow. In the left panel, absorption features are slightly stronger for the green line, thus in the in-scattering region, the retrieved

NO_2 concentration is expected to be higher near the cloud edge compared to a pixel further away from cloud edge.

3.4 NO2 retrieval for box cloud base case

The NO2 retrieval algorithm has been applied to the synthetic spectra. The left plot in Fig. 26 shows the results for the Pacific polluted NO2 scenario. Here we obtain a small offset to the true value, which is similar in clearsky and cloudy pixels. This result shows, that the simplified cloud treatment of the NO2 retrieval algorithm works very well for this particular test case. The retrieval result is generally not much influenced by the cloud. The right plot in Fig. 26 shows the results for the European polluted scenario. Here we find that the result is strongly influenced by 3D cloud scattering. We get an overestimation of the NO2 vertical column density for the in-scattering region and an underestimation in the cloud shadow. For bright cloudy pixels we also find a clear overestimation of the NO2 concentration. Obviously, the simplified cloud treatment in the NO2 retrieval algorithm can not well handle cases with a large amount of NO2 is in the lower atmosphere. In order to better understand the retrieval biases, intermediate retrieval parameters are shown in the Appendix (Fig. 33 and Fig. 34).

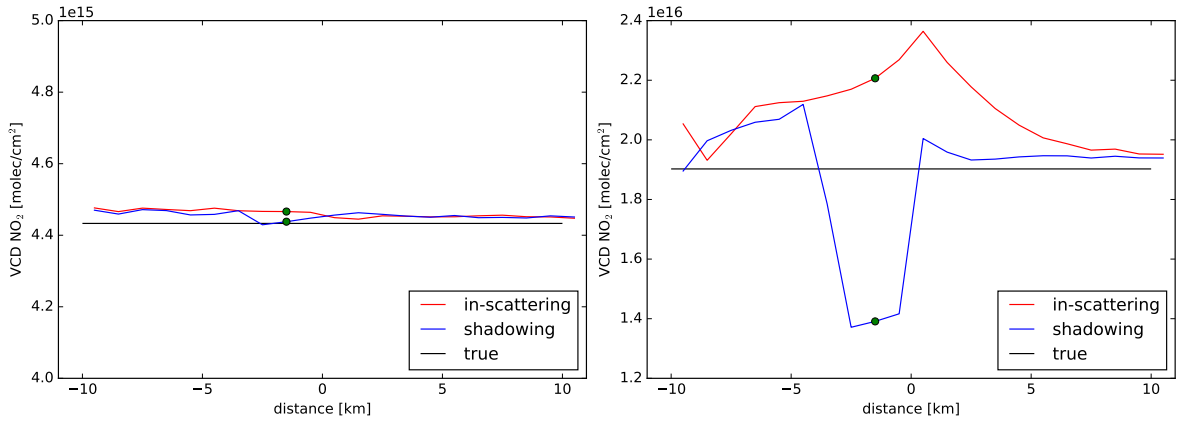

Figure 26: Retrieval results for the base case. The retrieved NO2 vertical column density is shown as a function of distance from the cloud edge. *Left:* Pacific polluted scenario. *Right:* European polluted scenario.

3.5 Sensitivity study based on box-cloud scenario

We would like to understand the dependence of the retrieval bias due to 3D cloud scattering for various parameters. To study this, we generated synthetic spectra for the pixel at a distance from 1-2 km from the cloud edge (marked by green circles in Fig. 26) for various cloud optical thicknesses (COT), cloud geometrical heights (CGH), solar zenith angles (SZA) and surface albedos.

Reflectances at 400 nm and 755 nm as a function of solar zenith angle and surface albedo are shown in Fig. 27. The dependencies on cloud optical and geometrical thickness are shown in Fig. 28.

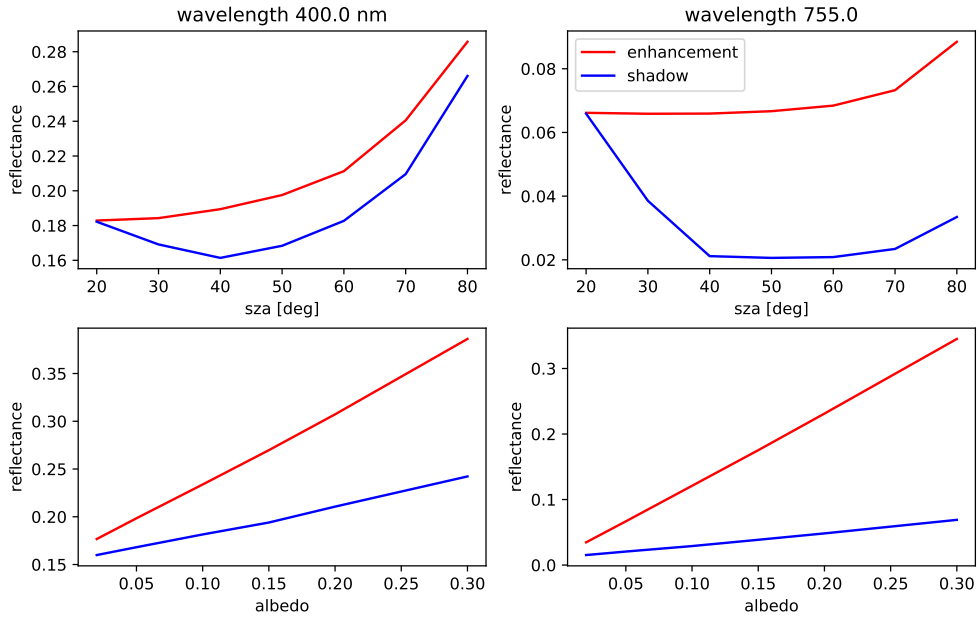

Figure 27: Reflectances as a function of solar zenith angle (top) and surface albedo (bottom). The left panels are for 400 nm and the right panels for 755 nm.

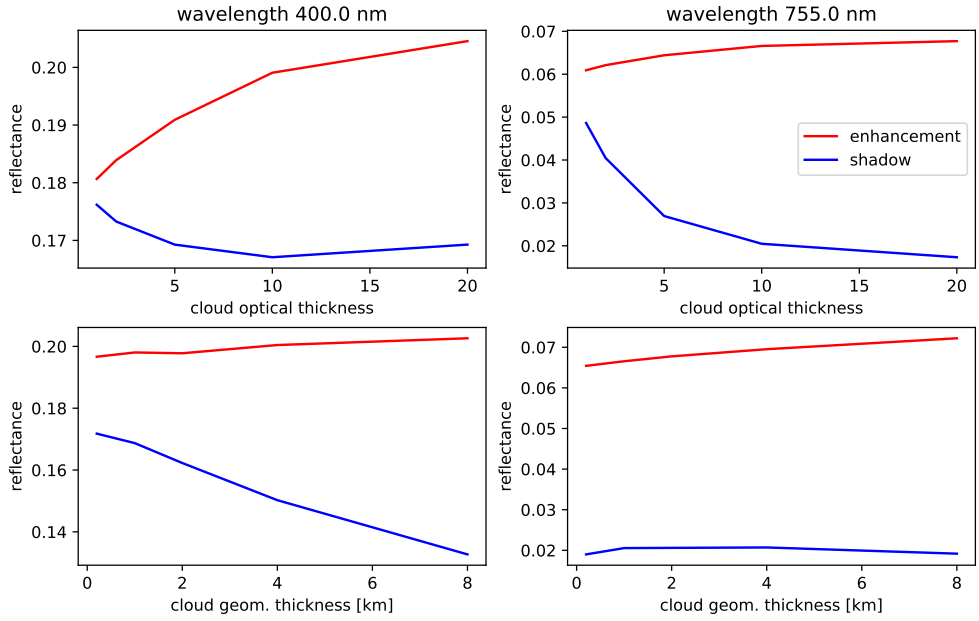

Figure 28: Reflectances as a function of cloud optical thickness (top) and cloud geometrical thickness (bottom). The left panels are for 400 nm and the right panels for 755 nm.

The retrieval biases for the Pacific polluted case are shown in Fig. 29. Generally the retrieved NO2-VCD agrees very well to the true value with differences mostly smaller than 1%. The largest difference of about 2% is found for a surface albedo of 0.3 in the cloud shadow.

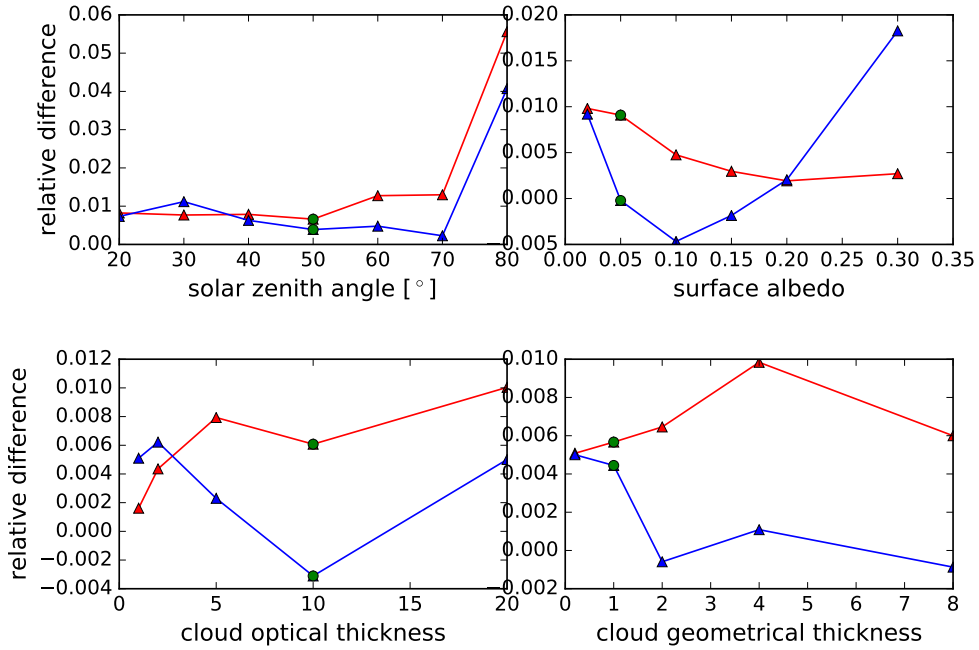

Figure 29: NO2 VCD retrieval bias for the Pacific polluted scenario due to 3D cloud scattering as a function of solar zenith angle (upper left), surface albedo (upper right), cloud optical thickness (lower left) and cloud geometrical thickness (lower right). The green circles correspond to the base case.

The retrieval biases for the European polluted scenario are presented in Fig. 30. Here we find much larger errors and clear dependencies on the various parameters.

Interestingly, the NO2 VCD in the cloud shadow is overestimated by more than 15% for SZA=20° and underestimated for SZA>=30°. For SZA=30° the retrieved VCD is about 10% smaller than the true VCD. The underestimation increases to more than 30% for SZA=70° and deceases again to about 25% for SZA=80°. The bias due to in-scattering decreases from about 18% for SZA=20° to about 8% for SZA=80°.

In the in-scattering region, the overestimation of NO2-VCD increases with increasing surface albedo from about 12% for an absorbing surface to almost 30% for a surface albedo of 0.3. The underestimation in the cloud shadow is maximal for a surface albedo of 0.05. Interestingly the error becomes very small for surface albedo 0.3 for the pixel including the cloud shadow.

With increasing COT the underestimation error in the cloud shadow increases continuously, the maximum value for COT=20 is about 32%. The overestimation error slightly increases with COT from 10% for COT=1 to 16% for COT=20. Increasing the CGH also increases the overestimation. The underestimation in the cloud shadow is decreased from about 30% for a very thin cloud (100 m) to about 20% for a very thick cloud (8 km).

Intermediate retrieval parameters for all results shown here are included in the Appendix.

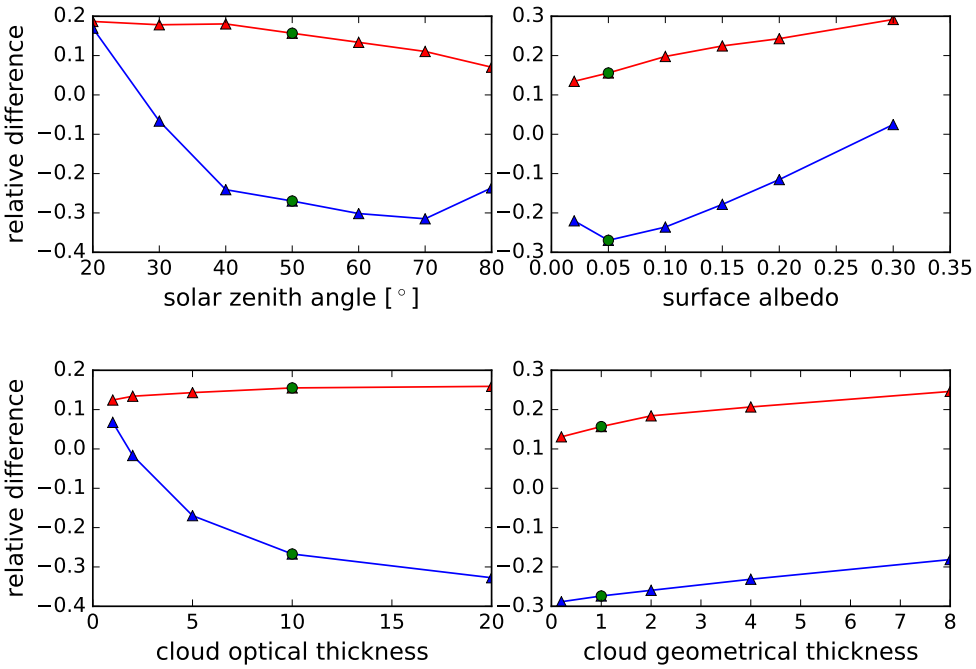

Figure 30: Same as Fig. 29 but for the European polluted scenario.

4 Retrieval of NO2 for partially cloudy pixels

In the previous Section 3 we have presented a study about the impact of 3D cloud scattering effects in pixels which are completely clear and are influenced by clouds in neighboring pixels. In reality, Sentinel5/TROPOMI pixels with a spatial resolution of about $7\times7\text{km}^2$ are mostly partially cloudy. Therefore, we plan to investigate the impact of 3D cloud scattering on NO2 retrievals for partially cloudy pixels and test, how simple cloud correction schemes can correct for subpixel clouds. We have defined a number of test cases. MYSTIC simulations of nadir reflectances for these test scenarios are shown in Fig. 31.

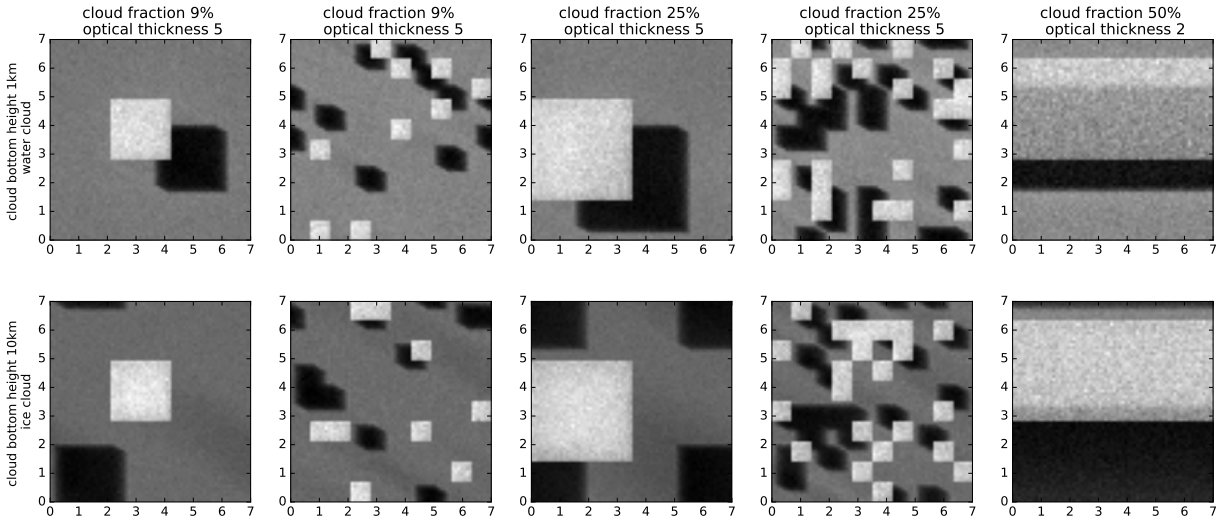

Figure 31: Test scenarios to study the impact of sub-pixel clouds on NO2-VCD retrievals.

5 Retrieval of NO2 for cases including realistic cloud scenes

In order to quantify the impact of 3D cloud scattering on NO2-VCD retrievals more generally for real world data, we will generate synthetic observations for larger scenes over Europe, the typical cloud scenarions defined in WP100 which cover all different types of clouds. In WP100, we have shown that LES simulations (ICON; Dipankar et al. (2015); Zängl et al. (2015); Heinze et al. (2017)) produce realistic clouds, for which various cloud feature metrics (CFMs) are statistically comparable to VIIRS observations. As an example, Figure 23 shows a simulated MODIS-like satellite image which has been generated using a fast radiative transfer model (Scheck et al., 2016, 2018). with cloud fields generated by the ICON LES model. Such cloud fields will be used as input for 3D MYSTIC simulations of spectra in the visible spectral range and in the O2A band.

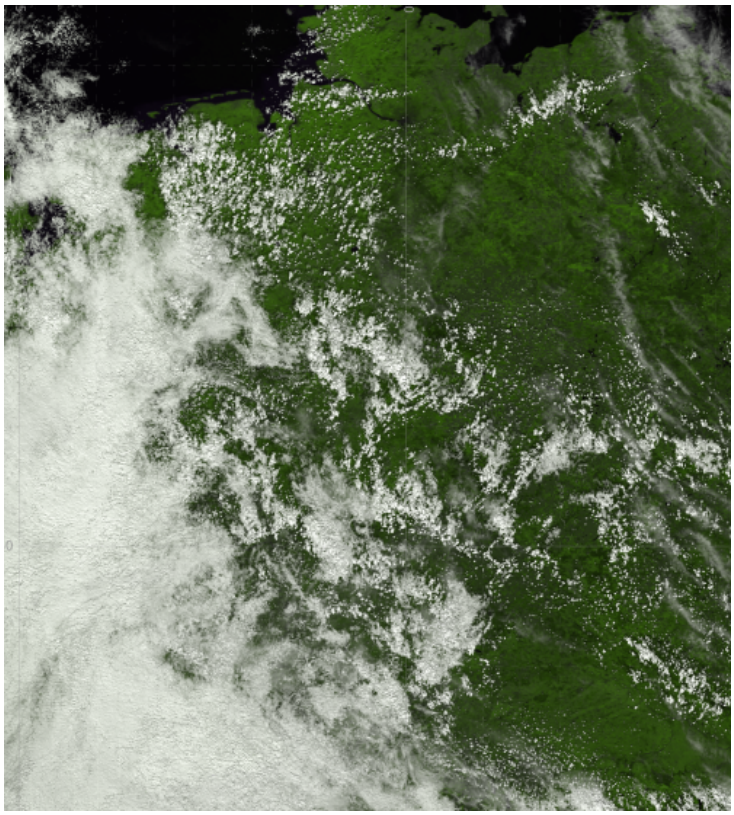

Figure 32: Simulation of a MODIS-like satellite image based on LES cloud fields (ICON) as input to the radiative transfer model (Scheck et al., 2016, 2018).

References

Blond, N., Boersma, K. F., Eskes, H. J., van der A, R. J., Van Roozendael, M., De Smedt, I., Bergametti, G., and Vautard, R.: Intercomparison of SCIAMACHY nitrogen dioxide observations, in situ measurements and air quality modeling results over Western Europe, Journal of Geophysical Research: Atmospheres, 112, doi:10.1029/2006JD007277, 2007.

Bodhaine, B. A., Wood, N. B., Dutton, E. G., and Slusser, J. R.: On Rayleigh optical depth calculations, J. Atm. Ocean Technol., 16, 1854–1861, 1999.

De Smedt, I., Müller, J.-F., Stavrakou, T., van der A, R., Eskes, H., and Van Roozendael, M.: Twelve years of global observations of formaldehyde in the troposphere using GOME and SCIAMACHY sensors, Atmospheric Chemistry and Physics, 8, 4947–4963, doi:10.5194/acp-8-4947-2008, https://www.atmos-chem-phys.net/8/4947/2008/, 2008.

Dipankar, A., Stevens, B., Heinze, R., Moseley, C., Zängl, G., Giorgetta, M., and Brdar, S.: Large eddy simulation using the general circulation model ICON, Journal of Advances in Modeling Earth Systems, 7, 963–986, doi:10.1002/2015MS000431, 2015.

Emde, C., Buras, R., and Mayer, B.: ALIS: An efficient method to compute high spectral resolution polarized solar radiances using the Monte Carlo approach, J. Quant. Spectrosc. Radiat. Transfer, 112, 1622–1631, 2011.

Emde, C., Buras-Schnell, R., Kylling, A., Mayer, B., Gasteiger, J., Hamann, U., Kylling, J., Richter, B., Pause, C., Dowling, T., and Bugliaro, L.: The libRadtran software package for radiative transfer calculations (version 2.0.1), Geophy. Mod. Dev., 9, 1647–1672, doi:10.5194/gmd-9-1647-2016, http://www.geosci-model-dev.net/9/1647/2016/, 2016.

Eriksson, P., Buehler, S. A., Davis, C. P., Emde, C., and Lemke, O.: ARTS, the atmospheric radiative transfer simulator, Version 2, J. Quant. Spectrosc. Radiat. Transfer, 112, 1551–1558, 2011.

Heinze, R., Dipankar, A., Henken, C. C., Moseley, C., Sourdeval, O., Trömel, S., Xie, X., Adamidis, P., Ament, F., Baars, H., Barthlott, C., Behrendt, A., Blahak, U., Bley, S., Brdar, S., Brueck, M., Crewell, S., Deneke, H., Di Girolamo, P., Evaristo, R., Fischer, J., Frank, C., Friederichs, P., Göcke, T., Gorges, K., Hande, L., Hanke, M., Hansen, A., Hege, H.-C., Hoose, C., Jahns, T., Kalthoff, N., Klocke, D., Kneifel, S., Knippertz, P., Kuhn, A., van Laar, T., Macke, A., Maurer, V., Mayer, B., Meyer, C. I., Muppa, S. K., Neggers, R. A. J., Orlandi, E., Pantillon, F., Pospichal, B., Röber, N., Scheck, L., Seifert, A., Seifert, P., Senf, F., Siligam, P., Simmer, C., Steinke, S., Stevens, B., Wapler, K., Weniger, M., Wulfmeyer, V., Zängl, G., Zhang, D., and Quaas, J.: Large-eddy simulations over Germany using ICON: a comprehensive evaluation, Quarterly Journal of the Royal Meteorological Society, 143, 69–100, doi:10.1002/qj.2947, 2017.

Mayer, B.: Radiative transfer in the cloudy atmosphere, European Physical Journal Conferences, 1, 75–99, 2009.

Mayer, B. and Kylling, A.: Technical note: The libRadtran software package for radiative transfer calclations – description and examples of use, Atmos. Chem. Phys., 5, 1855–1877, 2005.

Scheck, L., Frerebeau, P., Buras-Schnell, R., and Mayer, B.: A fast radiative transfer method for the simulation of visible satellite imagery, Journal of Quantitative Spectroscopy and Radiative Transfer, 175, 54 – 67, doi:10.1016/j.jqsrt.2016.02.008, 2016.

Scheck, L., Weissmann, M., and Mayer, B.: Efficient Methods to Account for Cloud-Top Inclination and Cloud Overlap in Synthetic Visible Satellite Images, Journal of Atmospheric and Oceanic Technology, 35, 665–685, doi:10.1175/JTECH-D-17-0057.1, 2018.

Serdyuchenko, A., Gorshelev, V., Weber, M., Chehade, W., and Burrows, J. P.: High spectral resolution ozone absorption cross-sections – Part 2: Temperature dependence, Atmos. Meas. Tech., 7, 625–636, doi:10.5194/amt-7-625-2014, https://www.atmos-meas-tech.net/7/625/2014/, 2014.

Spurr, R. J.: VLIDORT: A linearized pseudo-spherical vector discrete ordinate radiative transfer code for forward model and retrieval studies in multilayer multiple scattering media, J. Quant. Spectrosc. Radiat. Transfer, 102, 316–342, 2006.

Thalman, R. and Volkamer, R.: Temperature Dependent Absorption Cross-Sections of O2-O2 collision pairs between 340 and 630 nm at atmospherically relevan pressure, Phys. Chem. Chem. Phys., p. doi:10.1039/C3CP50968K, 2013.

Vandaele, A., Hermans, C., Simon, P., Carleer, M., Colin, R., Fally, S., Merienne, M., Jenouvrier, A., and Coquart, B.: Measurements of the NO_2 absorption cross-section from 42000 cm-1 to 10 000 cm-1 (238–1000 nm) at 220 K and 294 K, J. Quant. Spectrosc. Radiat. Transfer, 59, 171 – 184, doi:10.1016/S0022-4073(97)00168-4, atmospheric Spectroscopy Applications 96, 1998.

Zängl, G., Reinert, D., Ripodas, P., and Baldauf, M.: The ICON (ICOsahedral Non-hydrostatic) modelling framework of DWD and MPI-M: Description of the non-hydrostatic dynamical core, Quarterly Journal of the Royal Meteorological Society, 141, 563–579, doi:10.1002/qj.2378, 2015.

A Appendix

A.1 NO2 retrieval parameters for box-cloud case

In this section the following intermediate retrieval parameters are plotted:

- NO2 slant column density, error bars correspond to the fitting error
- air mass factor (solid lines are cloud corrected, dashed lines correspond to clearsky air mass factors)

- Effective O2-O2 cloud fraction
- Derived O2-O2 cloud height
- O4 slant column density
- Residual of cloud fitting

The blue lines are for pixels including cloud shadow and the red lines for pixels which are brighter due to cloud scattering.

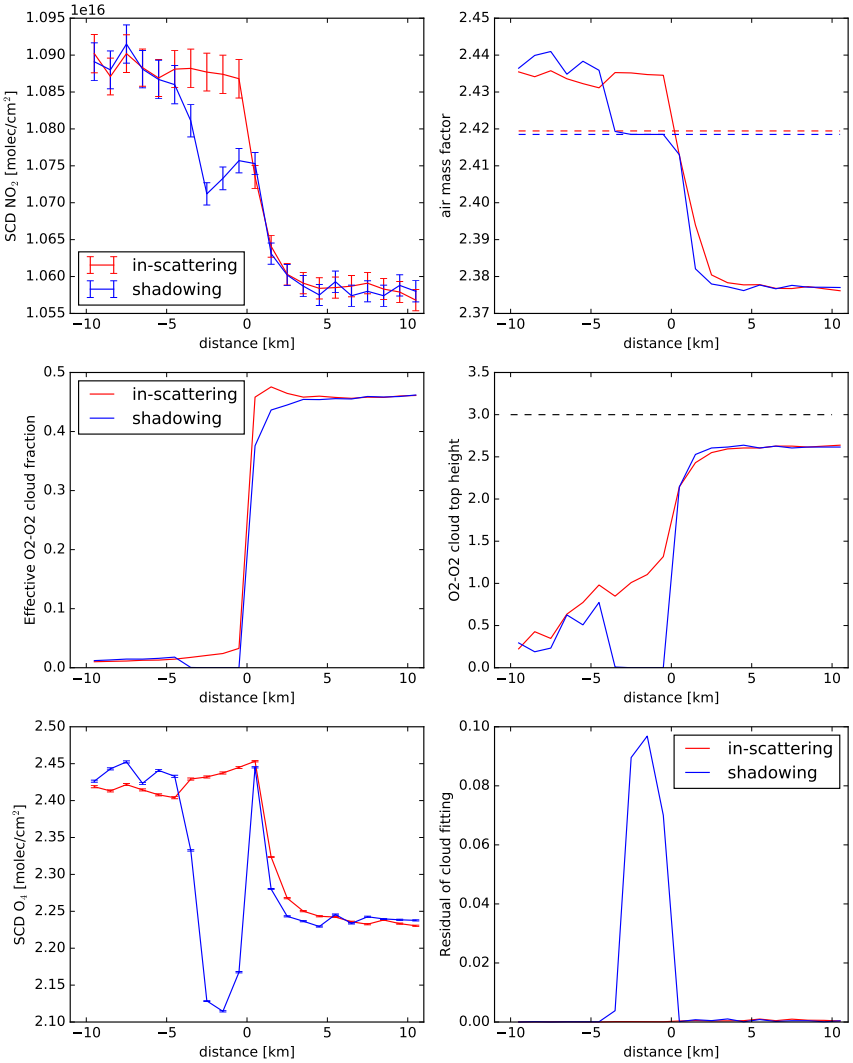

Figure 33: Retrieval parameters for box cloud scenario, base case, Pacific polluted NO2 profile.

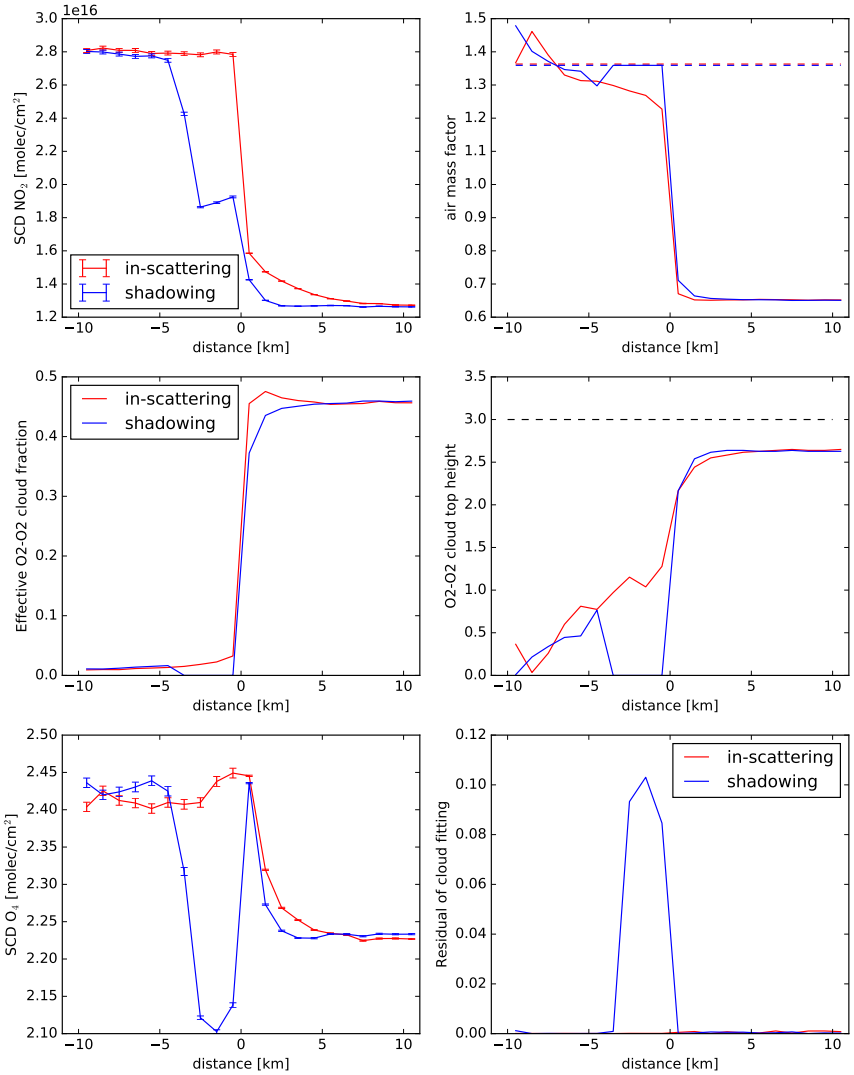

Figure 34: Retrieval parameters for box cloud scenario, base case, European polluted NO2 profile.

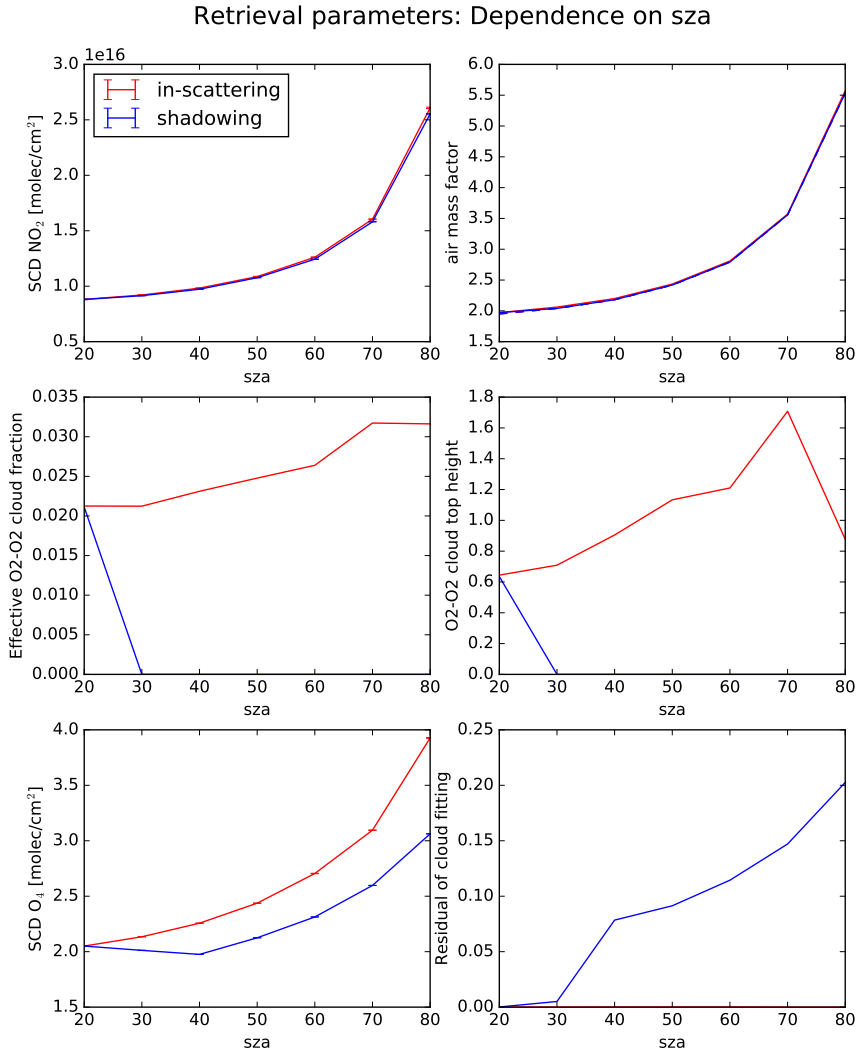

Figure 35: Dependence of retrieval parameters on solar zenith angle (sza) for Pacific polluted NO2 profile.

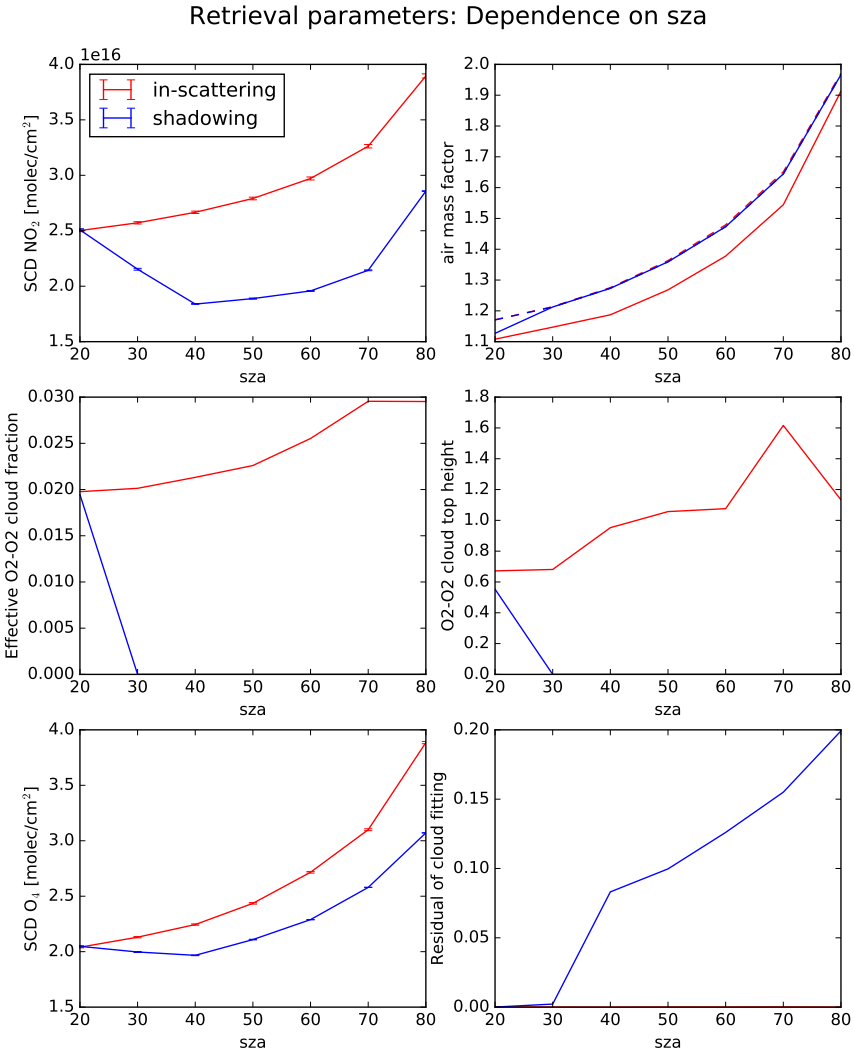

Figure 36: Dependence of retrieval parameters on solar zenith angle (sza) for Pacific polluted NO2 profile.

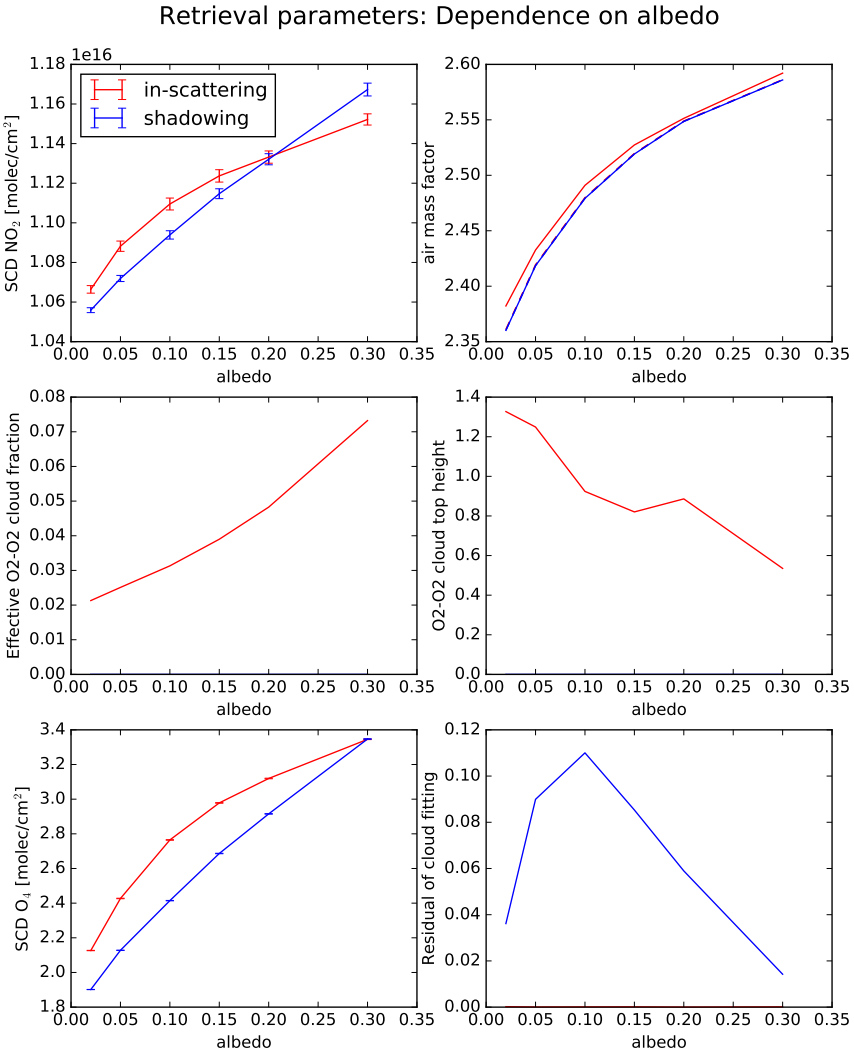

Figure 37: Dependence of retrieval parameters on surface albedo for Pacific polluted NO2 profile.

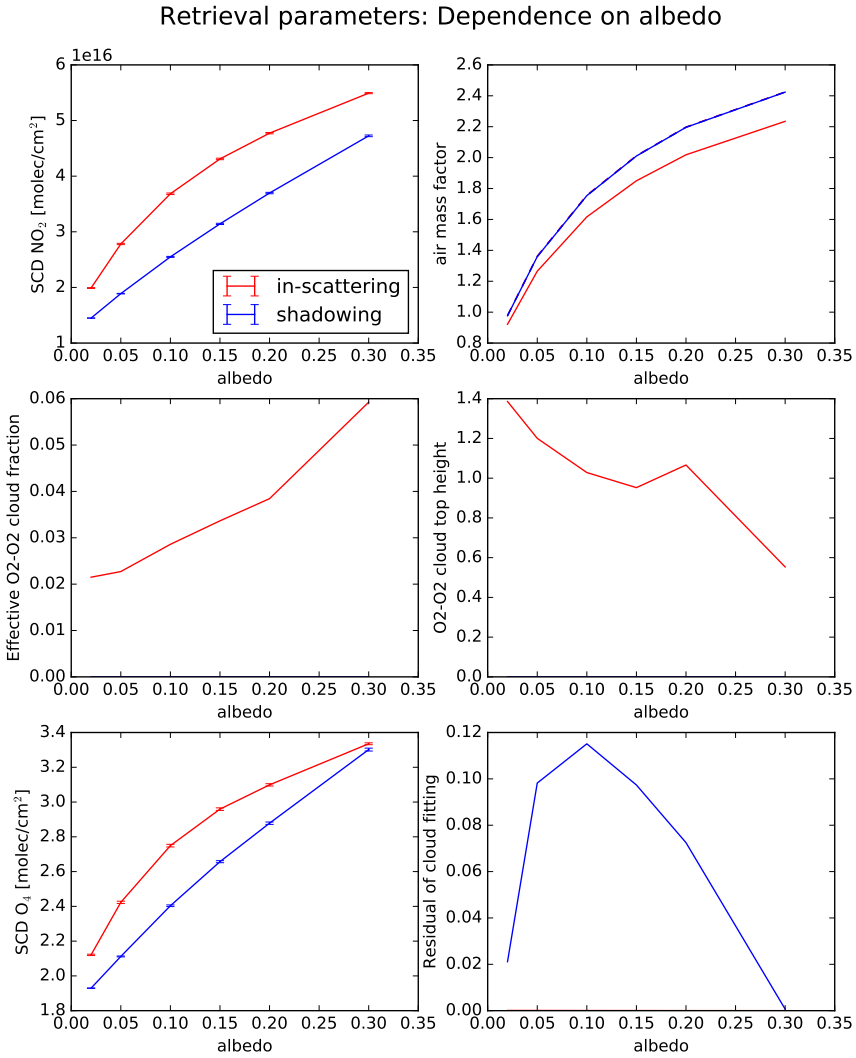

Figure 38: Dependence of retrieval parameters on surface albedo for Pacific polluted NO2 profile.

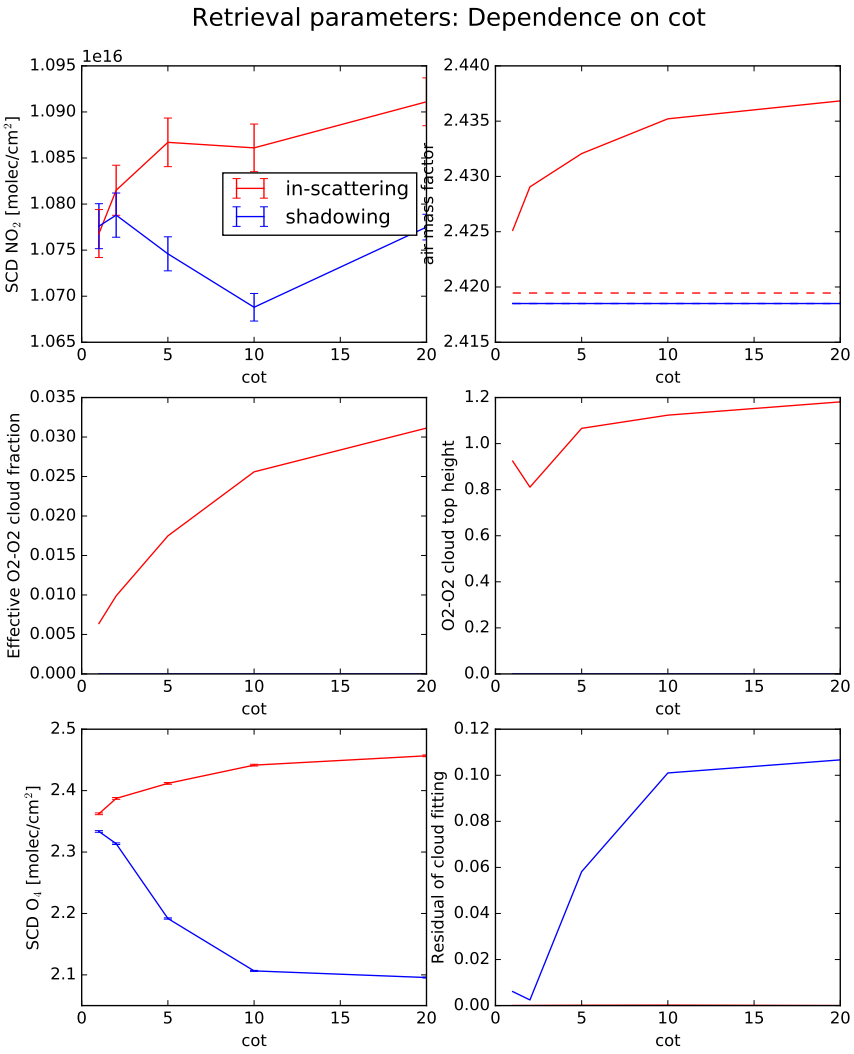

Figure 39: Dependence of retrieval parameters on cloud optical thickness for Pacific polluted NO2 profile.

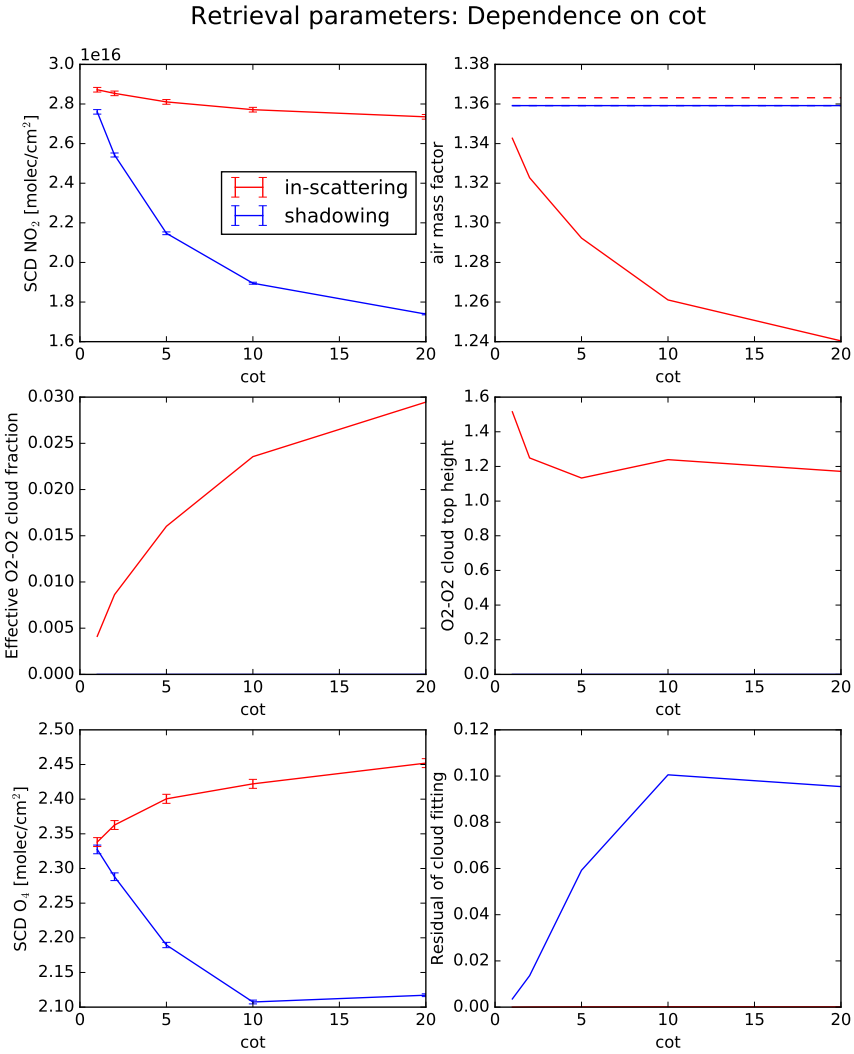

Figure 40: Dependence of retrieval parameters on cloud optical thickness for Pacific polluted NO2 profile.

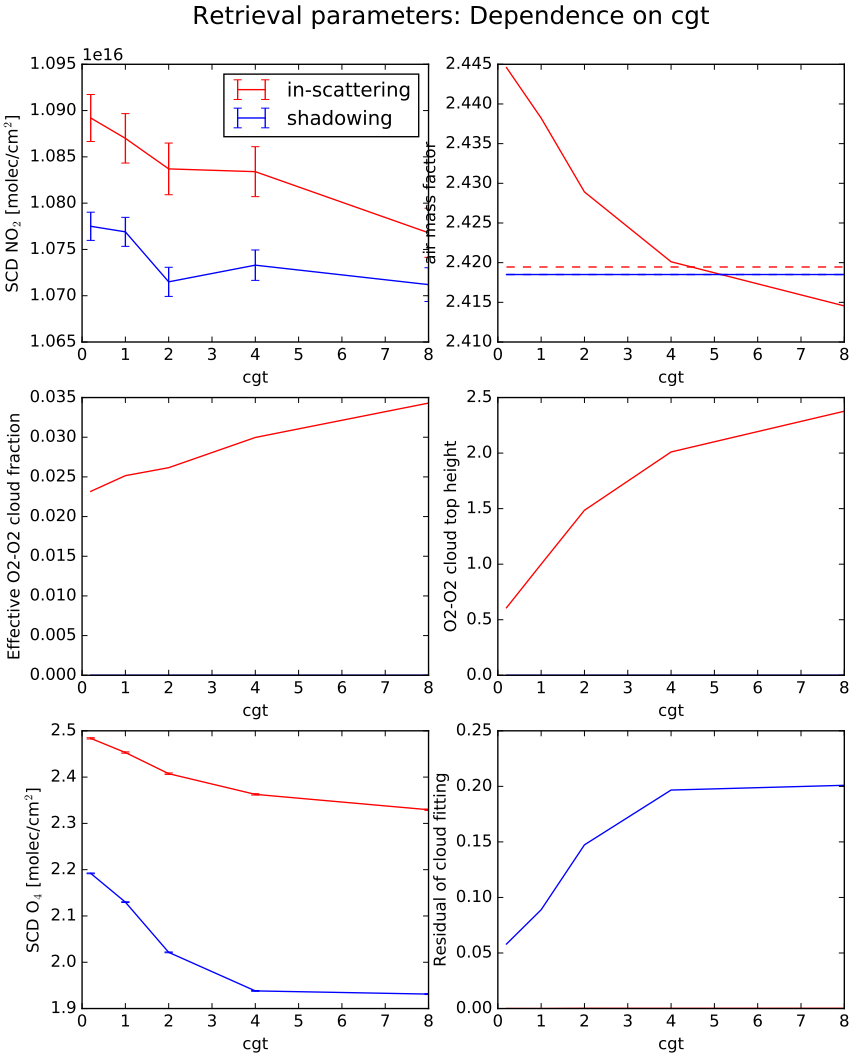

Figure 41: Dependence of retrieval parameters on cloud geometrical thickness for Pacific polluted NO2 profile.

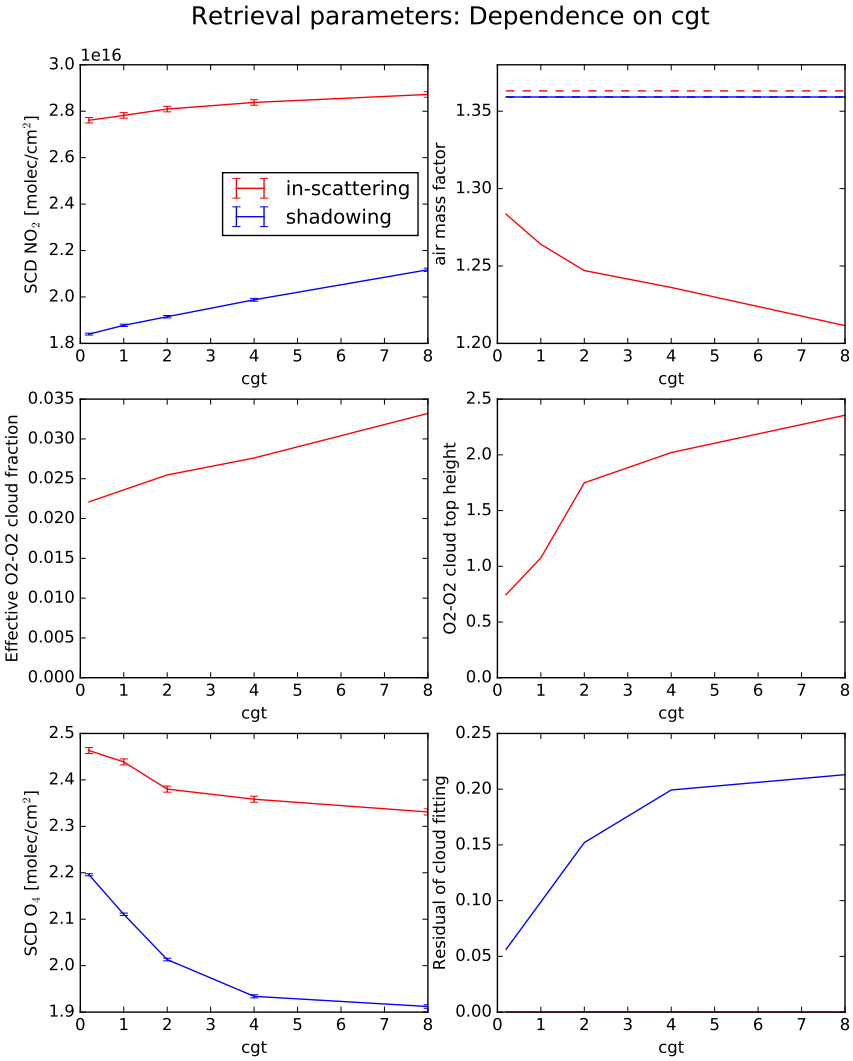

Figure 42: Dependence of retrieval parameters on cloud geometrical thickness for Pacific polluted NO2 profile.